Transonic Corrections for the Unsteady Compressible Source and Doublet Panel Method

Grigorios Dimitriadis,* Adrien Crovato,† and Mariano Sánchez Martínez‡
University of Liège, 4000 Liège, Belgium
Vito Laraspata§ and Leonardo Soria¶
Polytecnic University of Bari, 70126 Bari, Italy
and
Spyridon Kilimtzidis** and Vassilis Kostopoulos††
University of Patras, 26504 Patras, Greece

https://doi.org/10.2514/1.C038024

The steady and unsteady aerodynamic predictions of the Doublet Lattice Method (DLM) are routinely corrected for camber, twist, and transonic effects using steady reference data obtained from experiments or higher-fidelity calculations. In this work, a novel correction technique is presented for the unsteady compressible Source and Doublet Panel Method (SDPM) in order to correct for transonic effects. Although the SDPM is more computationally expensive than the DLM, it can predict complete steady and oscillatory pressure distributions around the entire surface of the exact geometry of a wing or body. Consequently, it does not require corrections for geometric properties such as camber and twist, only for transonic flow phenomena. The corrected predictions are compared to unsteady pressure distributions measured experimentally for two experimental test cases from the literature. It is shown that that the predictions of the SDPM correction method are accurate as long as the reference pressure data are of adequate quality. Finally, the SDPM with transonic correction is applied to the prediction of the flutter boundary of the AGARD 445.6 wing, and it is demonstrated that the proposed approach is capable of predicting the transonic dip.

I. Introduction

CORRECTIONS for camber, twist, and transonic effects have been applied to the steady and unsteady aerodynamic predictions of the Doublet Lattice Method (DLM) [1,2] since the 1970s [3]. Palacios et al. [4] presented a thorough review of the literature available on such corrections in 2001, but important developments have occurred since then, such as the successive kernel expansion technique [5]. As the DLM is a lifting surface method, it can only calculate the pressure jump across the surface of a wing that has been idealized as a flat surface. Alternatively, the unsteady compressible Source and Doublet Panel Method (SDPM) [6–8] can predict the pressure distribution around the entire surface of the exact geometry of a wing or body. As a consequence, it does not require corrections for camber or twist. On the other hand, both the DLM and the SDPM are based on the linearized small perturbation potential equation so that they cannot predict transonic flows accurately. Therefore, they both require correction when applied to such flow cases. This work presents a novel correction method for transonic effects developed specifically for the unsteady compressible SDPM.

Presented as Paper 2024-2146 at the AIAA SCITECH 2024 Forum, Orlando, FL, January 8–12, 2024; received 8 April 2024; accepted for publication 14 October 2024; published online 20 December 2024.

*Professor, Aerospace and Mechanical Engineering Department; gdimitiradis@uliege.be. Senior Member AIAA.
†Post-Doctoral Researcher, Aerospace and Mechanical Engineering Department; a.crovato@uliege.be.
‡Ph.D. Researcher, Aerospace and Mechanical Engineering Department; m.sanchezmartinez@uliege.be.
§Ph.D. Researcher, Department of Mechanics, Mathematics and Management; v.laraspata1@phd.poliba.it.
¶Associate Professor, Department of Mechanics, Mathematics and Management; leonardo.soria@poliba.it.
**Postdoctoral Researcher, Department of Mechanical Engineering & Aeronautics; s.kilimtzidis@upnet.gr.
††Professor, Department of Mechanical Engineering & Aeronautics; kostopoulos@upatras.gr.

II. Fundamentals of Transonic Correction Methods

Unsteady subsonic panel methods solve the linearized small disturbance equation

$$(1-M_\infty^2)\phi_{xx}+\phi_{yy}+\phi_{zz}-\frac{2M_\infty}{a_\infty}\phi_{xt}-\frac{1}{a_\infty^2}\phi_{tt}=0 \tag{1}$$

where M_∞ and a_∞ are the freestream Mach number and speed of sound and ϕ is the perturbation velocity potential. If $M_\infty<1$, Eq. (1) can only describe subcritical flows, that is, flows where the local Mach number never exceeds 1. To model transonic flows with a subsonic M_∞ but locally supersonic conditions, the nonlinear full potential equation or transonic small disturbance (TSD) equations are required. The latter is given by

$$\left(1-M_\infty^2-\frac{\gamma+1}{U_\infty}M_\infty^2\phi_x\right)\phi_{xx}+\phi_{yy}+\phi_{zz}-\frac{2M_\infty}{a_\infty}\phi_{xt}-\frac{1}{a_\infty^2}\phi_{tt}=0 \tag{2}$$

where it is assumed that the freestream only has a U_∞ velocity component. Equation (2) is nonlinear and can be solved using either full discretization of the flowfield or a field-panel approach. An alternative solution can be obtained by linearizing the TSD equation in time. The perturbation potential is written as

$$\phi(\boldsymbol{x},t)=\bar{\phi}(\boldsymbol{x})+\phi'(\boldsymbol{x},t)$$

where $\bar{\phi}(\boldsymbol{x})$ is a solution of the steady TSD equation

$$\left(1-M_\infty^2-\frac{\gamma+1}{U_\infty}M_\infty^2\bar{\phi}_x\right)\bar{\phi}_{xx}+\bar{\phi}_{yy}+\bar{\phi}_{zz}=0 \tag{3}$$

and $\phi'(\boldsymbol{x},t)$ is a small time-varying potential, such that $\phi'(\boldsymbol{x},t)<<\bar{\phi}(\boldsymbol{x})$. Substituting into Eq. (2), enforcing Eq. (3), and neglecting products of small quantities leads to

$$(1-M_\infty^2)\phi'_{xx}+\phi'_{yy}+\phi'_{zz}-\frac{2M_\infty}{a_\infty}\phi'_{xt}-\frac{1}{a_\infty^2}\phi'_{tt}=\frac{\gamma+1}{U_\infty}M_\infty^2\frac{\partial}{\partial x}(\bar{\phi}_x\phi'_x) \quad (4)$$

Equation (4) is known as the time-linearized transonic small disturbance equation (TLTSD), because it is linear in ϕ'. The steady solution $\bar{\phi}$ can be obtained independently by solving either Eq. (3) or a higher-fidelity equation. It follows that, in order to obtain unsteady transonic potential solutions, only the steady flow component must be calculated from a nonlinear equation. The small unsteady flow component can be calculated by the linear equation (4), which is the time-linearized small disturbance equation with an additional linear term on the right-hand side. Here, the TLTSD was developed from the TSD for conciseness, but a similar analysis can be applied to the full potential equation.

The basis of transonic correction techniques for panel methods is the idea that solutions to Eq. (1) can be corrected using a known steady nonlinear solution in order to become solutions to Eq. (4), which is very similar. Furthermore, calculating the value of $\bar{\phi}_x$ in the entire flowfield is not necessary; most transonic correction techniques make use of the steady pressure distribution on the surface of a body or the steady aerodynamic loads acting on the body.

III. Transonic Correction for the Doublet Lattice Method

For a wing discretized into N flat panels, the steady doublet lattice method equation is given by

$$-\alpha_0 \boldsymbol{I}_{N,1}=\tilde{\boldsymbol{A}}(0)\Delta\boldsymbol{c}_p(0,\alpha_0) \quad (5)$$

where α_0 is the steady (or mean) angle of attack, $\boldsymbol{I}_{N,1}$ is a $N\times 1$ vector whose elements are all equal to 1, $\tilde{\boldsymbol{A}}(0)$ is the $N\times N$ DLM aerodynamic influence coefficient matrix at zero frequency, and $\Delta\boldsymbol{c}_p(0,\alpha_0)$ is the $N\times 1$ vector of pressure jumps across the surface at the panel control points. The value of $\Delta\boldsymbol{c}_p(0,\alpha_0)$ that will be obtained by solving Eq. (5) does not reflect the camber or twist of the wing and does not model transonic phenomena such as shock waves impinging on the surface, because the DLM is a purely subsonic technique. The first correction to be applied then concerns this steady pressure jump, such that both geometric and transonic effects are taken into account. Dropping the (0) notation for conciseness, Eq. (5) becomes

$$-\alpha \boldsymbol{I}_{N,1}=\tilde{\boldsymbol{A}}\Delta\boldsymbol{c}_p(\alpha) \quad (6)$$

It is now assumed that the correct pressure jump at a reference angle of attack α_{ref} is known and is denoted by $\Delta\boldsymbol{c}_p(\alpha_{\text{ref}})$. The objective is to calculate the pressure jump at a slightly higher angle $\alpha_{\text{ref}}+\Delta\alpha$. Applying a first-order Taylor expansion to $\Delta\boldsymbol{c}_p$ around α_{ref} leads to

$$\Delta\boldsymbol{c}_p(\alpha_{\text{ref}}+\Delta\alpha)=\Delta\boldsymbol{c}_p(\alpha_{\text{ref}})+\frac{\partial\Delta\boldsymbol{c}_p}{\partial\alpha}\Delta\alpha \quad (7)$$

The derivative $\partial\Delta\boldsymbol{c}_p/\partial\alpha$ can be calculated from the DLM solution by differentiating Eq. (6) with respect to α and then solving for $\partial\Delta\boldsymbol{c}_p/\partial\alpha$,

$$\frac{\partial\Delta\boldsymbol{c}_p}{\partial\alpha}=-\tilde{\boldsymbol{A}}^{-1}\boldsymbol{I}_{N,1} \quad (8)$$

noting that the steady global influence coefficient matrix $\tilde{\boldsymbol{A}}$ calculated by the DLM does not depend on the angle of attack. Nevertheless, Eq. (8) does not model all of the physics of the problem, because the DLM cannot represent shock waves. Therefore, $\tilde{\boldsymbol{A}}$ will be multiplied by a correction matrix $\boldsymbol{D}^{\text{corr}}$, such that

$$\Delta\boldsymbol{c}_p(\alpha_{\text{ref}}+\Delta\alpha)=\Delta\boldsymbol{c}_p(\alpha_{\text{ref}})-(\boldsymbol{D}^{\text{corr}}\tilde{\boldsymbol{A}})^{-1}\boldsymbol{I}_{N,1}\Delta\alpha \quad (9)$$

will yield an accurate pressure jump distribution $\Delta\boldsymbol{c}_p(\alpha_{\text{ref}}+\Delta\alpha)$, for every small $\Delta\alpha$.

Values for the elements of $\boldsymbol{D}^{\text{corr}}$ can be obtained if reliable pressure jump values at both α_{ref} and $\alpha_{\text{ref}}+\Delta\alpha$ are calculated using a higher-fidelity simulation method or measured experimentally. These reliable pressure values will be referred to as the reference pressures $\Delta\boldsymbol{c}_p^{\text{ref}}(\alpha_{\text{ref}})$ and $\Delta\boldsymbol{c}_p^{\text{ref}}(\alpha_{\text{ref}}+\Delta\alpha)$. Substituting them in Eq. (9) and rearranging leads to

$$\Delta\boldsymbol{c}_{p_\alpha}^{\text{ref}}=\frac{\Delta\boldsymbol{c}_p^{\text{ref}}(\alpha_{\text{ref}}+\Delta\alpha)-\Delta\boldsymbol{c}_p^{\text{ref}}(\alpha_{\text{ref}})}{\Delta\alpha}=-(\boldsymbol{D}^{\text{corr}}\tilde{\boldsymbol{A}})^{-1}\boldsymbol{I}_{N,1} \quad (10)$$

where $\Delta\boldsymbol{c}_{p_\alpha}^{\text{ref}}$ is the normalized reference pressure jump. Every term in this expression is known except for $\boldsymbol{D}^{\text{corr}}$. However, the dimensions of $\boldsymbol{D}^{\text{corr}}$ are $N\times N$, where N is the number of panels, while there are only N equations. This problem is usually sidestepped by defining $\boldsymbol{D}^{\text{corr}}$ as a diagonal matrix so that only its N diagonal elements have nonzero values. Solving Eq. (10) for these elements yields (see, for example, Ref. [9])

$$D_{I,I}^{\text{corr}}=-\frac{1}{\sum_{J=1}^{N}\tilde{A}_{I,J}\Delta c_{p_\alpha,J}^{\text{ref}}} \quad (11)$$

for $I=1,\ldots,N$. Then, the corrected DLM pressure jump at any value of α is given by Eq. (9),

$$\Delta\boldsymbol{c}_p(\alpha)=-(\boldsymbol{D}^{\text{corr}}\tilde{\boldsymbol{A}})^{-1}\boldsymbol{I}_{N,1}(\alpha-\alpha_{\text{ref}})+\Delta\boldsymbol{c}_p^{\text{ref}}(\alpha_{\text{ref}}) \quad (12)$$

as long as $\alpha-\alpha_{\text{ref}}$ is small.

The next step is to correct the unsteady pressure jump, $\Delta\boldsymbol{c}_p(\omega)$, which is a complex number. The magnitude of this pressure jump can be corrected easily using the steady correction technique, but the phase correction is more challenging. The successive kernel expansion technique [5] is a method designed to overcome this difficulty. The unsteady DLM equation can be written in matrix form as

$$\boldsymbol{w}(k)=\tilde{\boldsymbol{A}}(k)\Delta\boldsymbol{c}_p(k) \quad (13)$$

where $\boldsymbol{w}(k)$ is the $N\times 1$ vector of upwash values acting at the control points of the N panels due to the motion, $\tilde{\boldsymbol{A}}(k)$ is the $N\times N$ global influence coefficient matrix, $\Delta\boldsymbol{c}_p(k)$ is the pressure jump across the upper and lower surfaces of the wing at the panel control points, and k is the reduced frequency defined as

$$k=\frac{\omega c_0}{2Q_\infty}$$

with Q_∞ denoting the freestream airspeed and c_0 denoting a characteristic length, such as the root chord. Equation (13) is valid at all reduced frequency values, down to $k=0$. The basis of the successive kernel expansion technique is to expand $\boldsymbol{w}(k)$, $\tilde{\boldsymbol{A}}(k)$, and $\Delta\boldsymbol{c}_p(k)$ as power series in ik, such that

$$\boldsymbol{w}(k)=\boldsymbol{w}_0+\mathrm{i}k\boldsymbol{w}_1+(\mathrm{i}k)^2\boldsymbol{w}_2+\ldots \quad (14)$$

$$\tilde{\boldsymbol{A}}(k)=\tilde{\boldsymbol{A}}_0+\mathrm{i}k\tilde{\boldsymbol{A}}_1+(\mathrm{i}k)^2\tilde{\boldsymbol{A}}_2+\ldots \quad (15)$$

$$\Delta\boldsymbol{c}_p(k)=\Delta\boldsymbol{c}_{p_0}+\mathrm{i}k\Delta\boldsymbol{c}_{p_1}+(\mathrm{i}k)^2\Delta\boldsymbol{c}_{p_2}+\ldots \quad (16)$$

where $\tilde{\boldsymbol{A}}_0=\tilde{\boldsymbol{A}}(0)$ is the steady DLM influence coefficient matrix in Eq. (5). Substituting back into Eq. (13) leads to

$$\boldsymbol{w}_0+\mathrm{i}k\boldsymbol{w}_1=(\tilde{\boldsymbol{A}}_0+\mathrm{i}k\tilde{\boldsymbol{A}}_1+(\mathrm{i}k)^2\tilde{\boldsymbol{A}}_2)(\Delta\boldsymbol{c}_{p_0}+\mathrm{i}k\Delta\boldsymbol{c}_{p_1}+(\mathrm{i}k)^2\Delta\boldsymbol{c}_{p_2})$$

noting that, usually, $\boldsymbol{w}_2=0$. This procedure is based on a theoretical expansion of the DLM kernel by Watkins et al. [10]. Expanding the right-hand side and collecting orders of $(\mathrm{i}k)^i$ leads to

$$\boldsymbol{w}_0 + \mathrm{i}k\boldsymbol{w}_1 = \tilde{\boldsymbol{A}}_0\Delta\boldsymbol{c}_{p_0} + \mathrm{i}k(\tilde{\boldsymbol{A}}_0\Delta\boldsymbol{c}_{p_1} + \tilde{\boldsymbol{A}}_1\Delta\boldsymbol{c}_{p_0}) + (\mathrm{i}k)^2(\tilde{\boldsymbol{A}}_1\Delta\boldsymbol{c}_{p_1} + \tilde{\boldsymbol{A}}_0\Delta\boldsymbol{c}_{p_2} + \tilde{\boldsymbol{A}}_2\Delta\boldsymbol{c}_{p_0}) + \ldots$$

Equating coefficients of $(\mathrm{i}k)^i$ between the left- and right-hand sides yields

$$\begin{aligned}\boldsymbol{w}_0 &= \tilde{\boldsymbol{A}}_0\Delta\boldsymbol{c}_{p_0}\\ \boldsymbol{w}_1 &= \tilde{\boldsymbol{A}}_0\Delta\boldsymbol{c}_{p_1} + \tilde{\boldsymbol{A}}_1\Delta\boldsymbol{c}_{p_0}\\ \boldsymbol{0} &= \tilde{\boldsymbol{A}}_1\Delta\boldsymbol{c}_{p_1} + \tilde{\boldsymbol{A}}_0\Delta\boldsymbol{c}_{p_2} + \tilde{\boldsymbol{A}}_2\Delta\boldsymbol{c}_{p_0}\end{aligned} \tag{17}$$

Solving for $\Delta\boldsymbol{c}_{p_0}$, $\Delta\boldsymbol{c}_{p_1}$, and $\Delta\boldsymbol{c}_{p_2}$ results in

$$\begin{aligned}\Delta\boldsymbol{c}_{p_0} &= \tilde{\boldsymbol{A}}_0^{-1}\boldsymbol{w}_0\\ \Delta\boldsymbol{c}_{p_1} &= \tilde{\boldsymbol{A}}_0^{-1}(\boldsymbol{w}_1 - \tilde{\boldsymbol{A}}_1\tilde{\boldsymbol{A}}_0^{-1}\boldsymbol{w}_0)\\ \Delta\boldsymbol{c}_{p_2} &= -\tilde{\boldsymbol{A}}_0^{-1}(\tilde{\boldsymbol{A}}_2\tilde{\boldsymbol{A}}_0^{-1}\boldsymbol{w}_0 + \tilde{\boldsymbol{A}}_1\tilde{\boldsymbol{A}}_0^{-1}(\boldsymbol{w}_1 - \tilde{\boldsymbol{A}}_1\tilde{\boldsymbol{A}}_0^{-1}\boldsymbol{w}_0))\end{aligned}$$

The matrix $\tilde{\boldsymbol{A}}_0$ is the zero-frequency DLM influence coefficient matrix of Eq. (5) and can be corrected by multiplying it by the diagonal correction matrix $\boldsymbol{D}^{\mathrm{corr}}$ whose elements are given by Eq. (11). Then, the corrected pressure jumps are obtained from

$$\begin{aligned}\Delta\boldsymbol{c}_{p_0}^{\mathrm{corr}} &= (\boldsymbol{D}^{\mathrm{corr}}\tilde{\boldsymbol{A}}_0)^{-1}\boldsymbol{w}_0\\ \Delta\boldsymbol{c}_{p_1}^{\mathrm{corr}} &= (\boldsymbol{D}^{\mathrm{corr}}\tilde{\boldsymbol{A}}_0)^{-1}(\boldsymbol{w}_1 - \tilde{\boldsymbol{A}}_1\tilde{\boldsymbol{A}}_0^{-1}\boldsymbol{w}_0)\\ \Delta\boldsymbol{c}_{p_2}^{\mathrm{corr}} &= -(\boldsymbol{D}^{\mathrm{corr}}\tilde{\boldsymbol{A}}_0)^{-1}(\tilde{\boldsymbol{A}}_2\tilde{\boldsymbol{A}}_0^{-1}\boldsymbol{w}_0 + \tilde{\boldsymbol{A}}_1\tilde{\boldsymbol{A}}_0^{-1}(\boldsymbol{w}_1 - \tilde{\boldsymbol{A}}_1\tilde{\boldsymbol{A}}_0^{-1}\boldsymbol{w}_0))\end{aligned} \tag{18}$$

noting that not all instances of $\tilde{\boldsymbol{A}}_0$ need to be corrected. The corrected pressure jump distribution is obtained by substituting $\Delta\boldsymbol{c}_{p_0}$, $\Delta\boldsymbol{c}_{p_1}$, and $\Delta\boldsymbol{c}_{p_2}$ into Eq. (16). The coefficients $\tilde{\boldsymbol{A}}_0$, $\tilde{\boldsymbol{A}}_1$, and $\tilde{\boldsymbol{A}}_2$ in expression (15) can be evaluated by calculating $\tilde{\boldsymbol{A}}(k)$ at three values of the reduced frequency, including $k = 0$, and then curve fitting the elements of the resulting matrices by a second-order polynomial in $\mathrm{i}k$.

IV. Transonic Correction for the Source and Doublet Panel Method

The SDPM first developed by Morino [6] differs from the DLM in that it represents the exact geometry of wings and bodies and must include a wake model. Martínez et al. [11] have shown that its steady and unsteady pressure distribution predictions can be improved by means of a nonlinear calculation of the pressure coefficient in purely subsonic conditions. However, the method is still not capable of modeling transonic flows and must be corrected to become effective in such conditions. For subsonic compressible flow, the SDPM solves the linearized small disturbance Eq. (1) in the form

$$\beta^2\phi_{xx} + \phi_{yy} + \phi_{zz} - \frac{2M_\infty}{a_\infty}\phi_{xt} - \frac{1}{a_\infty^2}\phi_{tt} = 0 \tag{19}$$

where $\beta = \sqrt{1 - M_\infty^2}$ is the subsonic compressibility factor. The Prandtl–Glauert transformation is applied to this equation in order to allow the use of the incompressible form of the steady source and doublet solutions. After substituting $\xi = x/\beta, \eta = y, \zeta = z$, Eq. (19) becomes

$$\phi_{\xi\xi} + \phi_{\eta\eta} + \phi_{\zeta\zeta} - \frac{2M_\infty}{a_\infty\beta}\phi_{\xi t} - \frac{1}{a_\infty^2}\phi_{tt} = 0 \tag{20}$$

whose steady part is Laplace's equation.

Dimitriadis et al. [12,13] show that Green's theorem for the subsonic SDPM can be written in the frequency domain for a wing discretized into N panels as

$$\left(\bar{\boldsymbol{B}}_\phi(\omega) - \frac{1}{2}\boldsymbol{I} + \bar{\boldsymbol{C}}_\phi(\omega)\boldsymbol{P}_e(\omega)\boldsymbol{P}_c\right)\boldsymbol{\mu}(\omega) = -\bar{\boldsymbol{A}}_\phi(\omega)\boldsymbol{\sigma}(\omega) \tag{21}$$

where ω is the frequency and the $N \times N$ matrices $\bar{\boldsymbol{A}}_\phi(\omega)$, $\bar{\boldsymbol{B}}_\phi(\omega)$, and $\bar{\boldsymbol{C}}_\phi(\omega)$ are compressible unsteady influence coefficient matrices; $\bar{\boldsymbol{A}}_\phi(\omega)$ expresses the influence of the wing source panels on the wing panel's control points, $\bar{\boldsymbol{B}}_\phi(\omega)$ expresses that of the wing doublet panels on the wing control points, and $\bar{\boldsymbol{C}}_\phi(\omega)$ expresses that of the wake doublet panels on the wing control points. The $N \times N$ matrix $\boldsymbol{P}_c$ is a panel selector matrix used to formulate the Kutta condition, and the $N \times N$ $\boldsymbol{P}_e(\omega)$ matrix expresses the time delay of the influence of the wake panels on the wing control points. Expressions for all the matrices in Eq. (21) are given in the Appendix. Equation (21) is a system of N equations with N unknowns, the $N \times 1$ wing doublet strength vector $\boldsymbol{\mu}(\omega)$. The $N \times 1$ wing source strength vector is evaluated from the zero normal mass flux boundary condition

$$\boldsymbol{\sigma}(\omega) = \mathrm{i}\Omega M_\infty \boldsymbol{n}_\xi \circ \boldsymbol{\mu}(\omega) - \left(\frac{1}{\beta}\boldsymbol{u}_m(\omega) \circ \boldsymbol{n}_\xi + \boldsymbol{v}_m(\omega) \circ \boldsymbol{n}_\eta + \boldsymbol{w}_m(\omega) \circ \boldsymbol{n}_\zeta\right) \tag{22}$$

where $\Omega = \omega/a_\infty\beta$; $\circ$ denotes the Hadamard product, that is, element-by-element multiplication, the elements of the $N \times 1$ vectors $\boldsymbol{u}_m(\omega)$, $\boldsymbol{v}_m(\omega)$, and $\boldsymbol{w}_m(\omega)$ are the relative motion velocities at the panel control points; and the elements of the $N \times 1$ vectors $\boldsymbol{n}_\xi, \boldsymbol{n}_\eta$, and $\boldsymbol{n}_\zeta$ are the components of the unit normal vectors at the control points in Prandtl–Glauert coordinates.

The relative velocities between the wing and the flow $\boldsymbol{u}_m(\omega)$, $\boldsymbol{v}_m(\omega)$, $\boldsymbol{w}_m(\omega)$ are known functions of the wing's motion and the freestream. Consequently, Eqs. (21) and (22) can be solved for the doublet strengths $\boldsymbol{\mu}(\omega)$. The perturbation velocities on the control points are then evaluated by differentiating numerically $\boldsymbol{\mu}(\omega)$ on the surface of the wing, such that [12]

$$\boldsymbol{\phi}_x(\omega) = \boldsymbol{K}_x(\omega)\boldsymbol{\sigma}(\omega), \boldsymbol{\phi}_y(\omega) = \boldsymbol{K}_y(\omega)\boldsymbol{\sigma}(\omega), \boldsymbol{\phi}_z(\omega) = \boldsymbol{K}_z(\omega)\boldsymbol{\sigma}(\omega) \tag{23}$$

where $\boldsymbol{\phi}_x, \boldsymbol{\phi}_y$, and $\boldsymbol{\phi}_z$ are $N \times 1$ vectors whose elements are the three components of the perturbation velocity on the control points and

$$\begin{aligned}\boldsymbol{K}_x(\omega) &= -\frac{1}{\beta}((\boldsymbol{a}_1 \circ \boldsymbol{D}^m \oslash \Delta\boldsymbol{s}_m + \boldsymbol{a}_2 \circ \boldsymbol{D}^n\Delta\boldsymbol{s}_n)\boldsymbol{K}(\omega) - \boldsymbol{I}\boldsymbol{a}_3)\\ \boldsymbol{K}_y(\omega) &= (\boldsymbol{b}_1 \circ \boldsymbol{D}^m \oslash \Delta\boldsymbol{s}_m + \boldsymbol{b}_2 \circ \boldsymbol{D}^n \oslash \Delta\boldsymbol{s}_n)\boldsymbol{K}(\omega) - \boldsymbol{I}\boldsymbol{b}_3\\ \boldsymbol{K}_z(\omega) &= -((\boldsymbol{c}_1 \circ \boldsymbol{D}^m \oslash \Delta\boldsymbol{s}_m + \boldsymbol{c}_2 \circ \boldsymbol{D}^n \oslash \Delta\boldsymbol{s}_n)\boldsymbol{K}(\omega) - \boldsymbol{I}\boldsymbol{c}_3)\\ \boldsymbol{K}(\omega) &= \left(\bar{\boldsymbol{B}}_\phi(\omega) - \frac{1}{2}\boldsymbol{I} + \bar{\boldsymbol{C}}_\phi(\omega)\boldsymbol{P}_e(\omega)\boldsymbol{P}_c\right)^{-1}\bar{\boldsymbol{A}}_\phi(\omega)\end{aligned} \tag{24}$$

where $\oslash$ denotes element-by-element division; $\boldsymbol{a}_1, \boldsymbol{a}_2, \boldsymbol{a}_3, \boldsymbol{b}_1, \boldsymbol{b}_2, \boldsymbol{b}_3$, $\boldsymbol{c}_1, \boldsymbol{c}_2$, and $\boldsymbol{c}_3$ are $N \times 1$ vectors whose elements are functions of the tangent and normal vectors at the panel control points; $\boldsymbol{D}^m$ and $\boldsymbol{D}^n$ are $N \times N$ finite difference matrices in the chordwise and spanwise directions; and $\Delta\boldsymbol{s}_m$ and $\Delta\boldsymbol{s}_n$ are $N \times 1$ vectors whose elements are the chordwise and spanwise lengths of the panels. Expressions for all the terms in Eq. (24) are given in the Appendix.

A second-order approximation of the steady pressure distribution around the wing is calculated in terms of the perturbation velocities at $\omega = 0$ as

$$\boldsymbol{c}_p(0) = 1 - \frac{\boldsymbol{u}(0)^2 + \boldsymbol{v}(0)^2 + \boldsymbol{w}(0)^2}{Q_\infty^2} + \frac{M_\infty^2}{Q_\infty^2}\boldsymbol{\phi}_x(0)^2 \tag{25}$$

where $\boldsymbol{u}(0) = U_\infty + \boldsymbol{\phi}_x(0)$, $\boldsymbol{v}(0) = V_\infty + \boldsymbol{\phi}_y(0)$, $\boldsymbol{w}(0) = W_\infty + \boldsymbol{\phi}_z(0)$, and $(U_\infty, V_\infty, W_\infty)$ are the components of the freestream Q_∞. Dimitriadis et al. [12,13] give expressions for the oscillating pressure distribution for rigid-body motion of a wing parallel to its

flight dynamic degrees of freedom. The present work concentrates on sinusoidal pitching oscillations around point (x_f, y_f, z_f) at frequency ω_0, such that the oscillating pressure component at the fundamental frequency is simplified to

$$\begin{aligned}\boldsymbol{c}_p(\omega_0) = \boldsymbol{c}_{p_\alpha}(\omega_0)\alpha(\omega_0) + \mathrm{i}\omega\boldsymbol{c}_{p_{\dot\alpha}}(\omega_0)\alpha(\omega_0)\\ + (\mathrm{i}\omega_0)^2\boldsymbol{c}_{p_{\ddot\alpha}}(\omega_0)\alpha(\omega_0)\end{aligned} \tag{26}$$

where the Fourier transform of the pitching motion is given by

$$\alpha(\omega) = \alpha_0\delta(\omega) + \frac{\alpha_1}{2\mathrm{i}}\delta(\omega-\omega_0) - \frac{\alpha_1}{2\mathrm{i}}\delta(\omega+\omega_0) \tag{27}$$

δ is the Kronecker delta function; and $\boldsymbol{c}_{p_\alpha}$, $\boldsymbol{c}_{p_{\dot\alpha}}$, and $\boldsymbol{c}_{p_{\ddot\alpha}}$ are $N\times 1$ pressure derivative vectors

$$\begin{aligned}\boldsymbol{c}_{p_\alpha}(\omega_0) &= -Q_\infty\boldsymbol{C}_0(\omega_0)\boldsymbol{n}_\zeta - \frac{2}{Q_\infty}\boldsymbol{w}(0)\\ \boldsymbol{c}_{p_{\dot\alpha}}(\omega_0) &= \frac{1}{\beta}\boldsymbol{C}_0(\omega_0)(\boldsymbol{n}_\xi\circ\boldsymbol{z}_c) - \boldsymbol{C}_0(\omega_0)(\boldsymbol{n}_\zeta\circ\boldsymbol{x}_c) - Q_\infty\boldsymbol{C}_1(\omega_0)\boldsymbol{n}_\zeta\\ &\quad + \frac{2}{Q_\infty^2}\boldsymbol{u}(0)\circ\boldsymbol{z}_c - \frac{2}{Q_\infty^2}\boldsymbol{w}(0)\circ\boldsymbol{x}_c\\ \boldsymbol{c}_{p_{\ddot\alpha}}(\omega_0) &= \frac{1}{\beta}\boldsymbol{C}_1(\omega_0)(\boldsymbol{n}_\xi\circ\boldsymbol{z}_c) - \boldsymbol{C}_1(\omega_0)(\boldsymbol{n}_\zeta\circ\boldsymbol{x}_c)\end{aligned} \tag{28}$$

where

$$\begin{aligned}\boldsymbol{C}_0(\omega_0) &= \frac{2M_\infty^2}{Q_\infty^2}\boldsymbol{K}_x(\omega_0)\circ\boldsymbol{\phi}_x(0) - \frac{2}{Q_\infty^2}\boldsymbol{K}_x(\omega_0)\circ\boldsymbol{u}(0)\\ &\quad - \frac{2}{Q_\infty^2}\boldsymbol{K}_y(\omega_0)\circ\boldsymbol{v}(0) - \frac{2}{Q_\infty^2}\boldsymbol{K}_z(\omega_0)\circ\boldsymbol{w}(0)\\ \boldsymbol{C}_1(\omega_0) &= \frac{2}{Q_\infty^2}\boldsymbol{K}(\omega_0) - \frac{2M_\infty^2}{Q_\infty^3}\boldsymbol{K}(\omega_0)\circ\boldsymbol{\phi}_x(0)\end{aligned} \tag{29}$$

and the symbol $\circ$ is also used to denote element-by-element multiplication of each of the columns of a matrix by the same column vector. Note that the coordinates of the panel control points $\boldsymbol{x}_c$, $\boldsymbol{y}_c$, and $\boldsymbol{z}_c$ are centred around the pitching axis point (x_f, y_f, z_f).

Equations (25) and (26) constitute a complete solution of the SDPM problem for pitching oscillations of a wing in subsonic and subcritical flight conditions, that is, in shock-free flow. If the flow is transonic and features weak shock waves, the SDPM solution can be corrected using reference steady pressure distributions, $\boldsymbol{c}_p^{\mathrm{ref}}$ and $\boldsymbol{c}_{p_\alpha}^{\mathrm{ref}}$ measured or calculated at pitch angle α_{ref}. First, the steady pressure distribution of Eq. (25) is linearized such that

$$\boldsymbol{c}_p(0) = -2\frac{\boldsymbol{\phi}_x(0)}{Q_\infty} = \frac{2}{\beta Q_\infty}(\boldsymbol{A}_{12}\boldsymbol{K}(0) - \boldsymbol{I}\boldsymbol{a}_3)\boldsymbol{\sigma}(0) \tag{30}$$

where $\boldsymbol{A}_{12} = \boldsymbol{a}_1\circ\boldsymbol{D}^m \oslash \Delta\boldsymbol{s}_m + \boldsymbol{a}_2\circ\boldsymbol{D}^n\Delta\boldsymbol{s}_n$ and $\boldsymbol{\sigma}(0) = -(U_\infty\boldsymbol{n}_\xi/\beta + V_\infty\boldsymbol{n}_\eta + W_\infty\boldsymbol{n}_\zeta)$. For steady motion at pitch angle α_0 in a free-stream Q_∞, $U_\infty \approx Q_\infty$, $V_\infty = 0$, and $W_\infty = Q_\infty\alpha$. Substituting for $\boldsymbol{\sigma}(0)$ into Eq. (30) and taking the derivative with respect to α_0 leads to

$$\boldsymbol{c}_{p_\alpha}(0) = -\frac{2}{\beta}(\boldsymbol{A}_{12}\boldsymbol{K}(0) - \boldsymbol{I}\boldsymbol{a}_3)\boldsymbol{n}_\zeta \tag{31}$$

This value of $\boldsymbol{c}_{p_\alpha}(0)$ is inaccurate because it cannot represent flows with shocks. Equation (31) must therefore be corrected such that its left-hand side becomes $\boldsymbol{c}_{p_\alpha}^{\mathrm{ref}}$. One way of achieving this is to write

$$\boldsymbol{c}_{p_\alpha}^{\mathrm{ref}} = -\frac{2}{\beta}(\boldsymbol{A}_{12}\boldsymbol{D}^{\mathrm{corr}}\boldsymbol{K}(0) - \boldsymbol{I}\boldsymbol{a}_3)\boldsymbol{n}_\zeta \tag{32}$$

where $\boldsymbol{D}^{\mathrm{corr}}$ is the $N\times N$ diagonal SDPM correction matrix, different than the one developed for the DLM. Solving Eq. (32) directly for $\boldsymbol{D}^{\mathrm{corr}}$ requires the inversion of matrix $\boldsymbol{A}_{12}$, which can be rank deficient. Alternatively, taking advantage of the fact that $\boldsymbol{D}^{\mathrm{corr}}$ is diagonal, Eq. (32) can be rearranged into

$$\begin{aligned}-\frac{\beta}{2}\left(\boldsymbol{c}_{p_\alpha}^{\mathrm{ref}} - \frac{2}{\beta}\boldsymbol{I}\boldsymbol{a}_3\boldsymbol{n}_\zeta\right) &= \boldsymbol{A}_{12}((\boldsymbol{K}(0)\boldsymbol{n}_\zeta)\circ\boldsymbol{D}^{\mathrm{corr}})\\ &= (\boldsymbol{A}_{12}\circ(\boldsymbol{K}(0)\boldsymbol{n}_\zeta)^T)\mathrm{diag}(\boldsymbol{D}^{\mathrm{corr}})\end{aligned} \tag{33}$$

This expression can be solved for the elements of $\mathrm{diag}(\boldsymbol{D}^{\mathrm{corr}})$ after applying boundary conditions. If there are $2m$ chordwise panels and n spanwise panels and the panel arrangement is such that $i = 1,\ldots,n$ denote the lower trailing-edge panels and $i = (2m-1)n+1,\ldots,2mn$ denote the upper trailing-edge panels, the boundary conditions are $D_{i,i}^{\mathrm{corr}} = 1$ for $i = 1,\ldots,n$ and $i = (2m-1)n+1,\ldots,2mn$. These boundary conditions reflect the fact that the flow is assumed to be predicted accurately by the uncorrected SDPM at the trailing edge, which is reasonable for transonic flow with weak shocks lying on the surface of the wing. Equation (33) can be written in the form

$$\bar{\boldsymbol{A}}\,\bar{\boldsymbol{x}} = \bar{\boldsymbol{b}} \tag{34}$$

where $\bar{\boldsymbol{A}} = (\boldsymbol{A}_{12}\circ(\boldsymbol{K}(0)\boldsymbol{n}_\zeta)^T)$, $\bar{\boldsymbol{x}} = \mathrm{diag}(\boldsymbol{D}^{\mathrm{corr}})$, and $\bar{\boldsymbol{b}} = -(\beta/2)(\boldsymbol{c}_{p_\alpha}^{\mathrm{ref}} - (2/\beta)\boldsymbol{I}\boldsymbol{a}_3\boldsymbol{n}_\zeta)$ and matrices $\bar{\boldsymbol{A}}$, $\bar{\boldsymbol{x}}$ are partitioned as

$$\begin{pmatrix}\bar{\boldsymbol{A}}_1 & \bar{\boldsymbol{A}}_2 & \bar{\boldsymbol{A}}_3\end{pmatrix}\begin{pmatrix}\bar{\boldsymbol{x}}_1\\ \bar{\boldsymbol{x}}_2\\ \bar{\boldsymbol{x}}_3\end{pmatrix} = \bar{\boldsymbol{b}}$$

In this latest expression, subscript 1 refers to the n panels of the lower trailing edge, subscript 3 refers to the n panels of the upper trailing edge, and subscript 2 refers to all other panels. The only unknown is $\bar{\boldsymbol{x}}_2$, because $\bar{\boldsymbol{x}}_1 = \bar{\boldsymbol{x}}_3 = \boldsymbol{I}_{n\times 1}$. Consequently,

$$\bar{\boldsymbol{x}}_2 = \bar{\boldsymbol{A}}_2^+(\bar{\boldsymbol{b}} - \bar{\boldsymbol{A}}_1\boldsymbol{I}_{n\times 1} - \bar{\boldsymbol{A}}_3\boldsymbol{I}_{n\times 1})$$

where $\bar{\boldsymbol{A}}_2^+$ denotes the Moore–Penrose pseudoinverse of the $N\times(N-2n)$ matrix $\bar{\boldsymbol{A}}_2$. As the rank of the $N\times N$ matrix $\bar{\boldsymbol{A}}$ is $N-n$, removing $2n$ unknowns from Eq. (34) results in a full rank problem to be solved in a least-squares sense. Consequently,

$$\mathrm{diag}(\boldsymbol{D}^{\mathrm{corr}}) = \begin{pmatrix}\boldsymbol{I}_{n\times 1}\\ \bar{\boldsymbol{A}}_2^+(\bar{\boldsymbol{b}} - \bar{\boldsymbol{A}}_1\boldsymbol{I}_{n\times 1} - \bar{\boldsymbol{A}}_3\boldsymbol{I}_{n\times 1})\\ \boldsymbol{I}_{n\times 1}\end{pmatrix} \tag{35}$$

while all off-diagonal elements of matrix $\boldsymbol{D}^{\mathrm{corr}}$ are equal to zero.

Once $\boldsymbol{D}^{\mathrm{corr}}$ has been evaluated, the matrices in Eq. (24) can be corrected such that

$$\begin{aligned}\boldsymbol{K}_x^{\mathrm{corr}}(\omega) &= -\frac{1}{\beta}((\boldsymbol{a}_1\circ\boldsymbol{D}^m \oslash \Delta\boldsymbol{s}_m + \boldsymbol{a}_2\circ\boldsymbol{D}^n\Delta\boldsymbol{s}_n)\boldsymbol{K}^{\mathrm{corr}}(\omega) - \boldsymbol{I}\boldsymbol{a}_3)\\ \boldsymbol{K}_y^{\mathrm{corr}}(\omega) &= (\boldsymbol{b}_1\circ\boldsymbol{D}^m \oslash \Delta\boldsymbol{s}_m + \boldsymbol{b}_2\circ\boldsymbol{D}^n \oslash \Delta\boldsymbol{s}_n)\boldsymbol{K}^{\mathrm{corr}}(\omega) - \boldsymbol{I}\boldsymbol{b}_3\\ \boldsymbol{K}_z^{\mathrm{corr}}(\omega) &= -((\boldsymbol{c}_1\circ\boldsymbol{D}^m \oslash \Delta\boldsymbol{s}_m + \boldsymbol{c}_2\circ\boldsymbol{D}^n \oslash \Delta\boldsymbol{s}_n)\boldsymbol{K}^{\mathrm{corr}}(\omega) - \boldsymbol{I}\boldsymbol{c}_3)\\ \boldsymbol{K}^{\mathrm{corr}}(\omega) &= \boldsymbol{D}^{\mathrm{corr}}\left(\bar{\boldsymbol{B}}_\phi(\omega) - \frac{1}{2}\boldsymbol{I} + \bar{\boldsymbol{C}}_\phi(\omega)\boldsymbol{P}_e(\omega)\boldsymbol{P}_c\right)^{-1}\bar{\boldsymbol{A}}_\phi(\omega)\end{aligned} \tag{36}$$

The corrected steady perturbation velocities become

$$\begin{aligned}\boldsymbol{\phi}_x^{\mathrm{corr}}(0) &= -\frac{Q_\infty}{\beta}\boldsymbol{K}_x(0)\boldsymbol{n}_\xi - Q_\infty\boldsymbol{K}_x^{\mathrm{corr}}(0)\boldsymbol{n}_\zeta\alpha_0\\ \boldsymbol{\phi}_y^{\mathrm{corr}}(0) &= -\frac{Q_\infty}{\beta}\boldsymbol{K}_y(0)\boldsymbol{n}_\xi - Q_\infty\boldsymbol{K}_y^{\mathrm{corr}}(0)\boldsymbol{n}_\zeta\alpha_0\\ \boldsymbol{\phi}_z^{\mathrm{corr}}(0) &= -\frac{Q_\infty}{\beta}\boldsymbol{K}_z(0)\boldsymbol{n}_\xi - Q_\infty\boldsymbol{K}_z^{\mathrm{corr}}(0)\boldsymbol{n}_\zeta\alpha_0\end{aligned}$$

and the corrected total flow velocities $\boldsymbol{u}^{\text{corr}}(0) = U_\infty + \boldsymbol{\phi}_x^{\text{corr}}(0)$, $\boldsymbol{v}^{\text{corr}}(0) = V_\infty + \boldsymbol{\phi}_y^{\text{corr}}(0)$, and $\boldsymbol{w}^{\text{corr}}(0) = W_\infty + \boldsymbol{\phi}_z^{\text{corr}}(0)$. Note that only the terms relative to the steady upwash velocity $Q_\infty\alpha$ must be corrected. The corrected steady pressure distribution can be calculated from Eq. (25),

$$\boldsymbol{c}_p^{\text{corr}}(0) = 1 - \frac{\boldsymbol{u}^{\text{corr}}(0)^2 + \boldsymbol{v}^{\text{corr}}(0)^2 + \boldsymbol{w}^{\text{corr}}(0)^2}{Q_\infty^2} + \frac{M_\infty^2}{Q_\infty^2}\boldsymbol{\phi}_x^{\text{corr}}(0)^2 \tag{37}$$

but is not required because the steady reference pressure can be used instead.

The oscillatory pressure correction is obtained by adapting Eq. (29) such that

$$\begin{aligned}\boldsymbol{C}_0^{\text{corr}}(\omega_0) &= \frac{2M_\infty^2}{Q_\infty^2}\boldsymbol{K}_x^{\text{corr}}(\omega_0)\circ\boldsymbol{\phi}_x^{\text{corr}}(0) - \frac{2}{Q_\infty^2}\boldsymbol{K}_x^{\text{corr}}(\omega_0)\circ\boldsymbol{u}^{\text{corr}}(0)\\ &\quad - \frac{2}{Q_\infty^2}\boldsymbol{K}_y^{\text{corr}}(\omega_0)\circ\boldsymbol{v}^{\text{corr}}(0) - \frac{2}{Q_\infty^2}\boldsymbol{K}_z^{\text{corr}}(\omega_0)\circ\boldsymbol{w}^{\text{corr}}(0)\\ \boldsymbol{C}_1^{\text{corr}}(\omega_0) &= \frac{2}{Q_\infty^2}\boldsymbol{K}^{\text{corr}}(\omega_0) - \frac{2M_\infty^2}{Q_\infty^3}\boldsymbol{K}^{\text{corr}}(\omega_0)\circ\boldsymbol{\phi}_x^{\text{corr}}(0)\end{aligned} \tag{38}$$

Then, the pressure derivatives of Eq. (28) become

$$\begin{aligned}\boldsymbol{c}_{p_\alpha}^{\text{corr}}(\omega_0) &= -Q_\infty\boldsymbol{C}_0^{\text{corr}}(\omega_0)\boldsymbol{n}_\zeta - \frac{2}{Q_\infty}\boldsymbol{w}^{\text{corr}}(0)\\ \boldsymbol{c}_{p_{\dot\alpha}}^{\text{corr}}(\omega_0) &= \frac{1}{\beta}\boldsymbol{C}_0(\omega_0)(\boldsymbol{n}_\xi\circ\boldsymbol{z}_c) - \boldsymbol{C}_0^{\text{corr}}(\omega_0)(\boldsymbol{n}_\zeta\circ\boldsymbol{x}_c)\\ &\quad - Q_\infty\boldsymbol{C}_1^{\text{corr}}(\omega_0)\boldsymbol{n}_\zeta + \frac{2}{Q_\infty^2}\boldsymbol{u}(0)\circ\boldsymbol{z}_c - \frac{2}{Q_\infty^2}\boldsymbol{w}^{\text{corr}}(0)\circ\boldsymbol{x}_c\\ \boldsymbol{c}_{p_{\ddot\alpha}}^{\text{corr}}(\omega_0) &= \frac{1}{\beta}\boldsymbol{C}_1(\omega_0)(\boldsymbol{n}_\xi\circ\boldsymbol{z}_c) - \boldsymbol{C}_1^{\text{corr}}(\omega_0)(\boldsymbol{n}_\zeta\circ\boldsymbol{x}_c)\end{aligned} \tag{39}$$

where, again, only the terms relative to the upwash ($\boldsymbol{n}_\zeta$ direction) have been corrected. Finally, the corrected oscillating pressure is calculated from Eq. (26):

$$\begin{aligned}\boldsymbol{c}_p^{\text{corr}}(\omega_0) &= \boldsymbol{c}_{p_\alpha}^{\text{corr}}(\omega_0)\alpha(\omega_0) + \mathrm{i}\omega\boldsymbol{c}_{p_{\dot\alpha}}^{\text{corr}}(\omega_0)\alpha(\omega_0)\\ &\quad + (\mathrm{i}\omega_0)^2\boldsymbol{c}_{p_{\ddot\alpha}}^{\text{corr}}(\omega_0)\alpha(\omega_0)\end{aligned} \tag{40}$$

V. Benchmark Supercritical Wing

The first application of the SDPM correction technique concerns the pitching oscillations of the Benchmark SuperCritical Wing (BSCW) [14], a rectangular half-wing model with root chord $c_0 = 0.406$ m, half-span $b/2 = 0.813$ m, full aspect ratio $AR = 4$ and a NASA SC(2)-0414 airfoil section. The wing was placed in NASA's Transonic Dynamics Tunnel and forced to oscillate in pitch around an axis passing through $x_f/c_0 = 0.5$, $y_f = 0$, $z_f = 0$. Steady and unsteady pressures were measured at a spanwise section lying at $y/(b/2) = 0.6$ at $M_\infty = 0.5$, 0.7, and 0.85. The tested oscillation frequencies lie between $f = 1$ Hz and 30 Hz, and the pitch amplitudes lie between $\alpha_1 = 0.17°$ and 1°. The mean pitch angle was $\alpha_0 = 5°$.

The reference pressure data were obtained by means of steady Reynolds-averaged Navier–Stokes (RANS) simulations carried out using ANSYS Fluent 2023. A finite volume discretization was applied to a computational domain extending $100c_0$ in all directions. A fine mesh of 13.7 million cells was used, leading to an y^+ value of around 0.26. The spatial convection terms were discretized using second-order upstream schemes and the spatial diffusion and source terms using central differences. A Green–Gauss function was selected for the calculation of gradients, and a steady-state solver was used with an iteration limit of 500 due to limited computational resources. Both the $k-\omega$ SST and Spalart–Allmaras turbulence models were tested, with different values of the turbulence intensity and turbulent viscosity ratio, respectively. The $k-\omega$ SST model with a value of turbulent intensity and viscosity ratio equal to 0.1 demonstrated better shockwave location and magnitude prediction characteristics with respect to the experimental data and was thus retained for the present study. Two sets of simulations were carried out, one set at $M_\infty = 0.7$ and $\alpha_0 = 4.5°$, $\alpha_0 = 5°$, and $\alpha_0 = 5.5°$ and one set at $M_\infty = 0.85$ and $\alpha_0 = 4.5°$, $\alpha_0 = 5°$, and $\alpha_0 = 5.5°$.

Figure 1a compares the pressure distribution predicted by the RANS simulation at $\alpha_0 = 5°$ and $M_\infty = 0.7$ with the experimental data reported by Piatak and Cleckner [14]. The agreement is quite good everywhere except in the neighborhood of the shock wave. The RANS simulation predicts that the shock occurs farther downstream than the experimental observations. Figure 1b plots the simulated and experimental pressure distributions for the same angle of attack but at $M_\infty = 0.85$. In this case, there are shocks both on the upper and lower surfaces. The location of the shock on the lower surface predicted by the RANS simulation may actually be correct, noting that the number of pressure taps on the lower surface is insufficient to accurately estimate the experimental position of the shock. On the other hand, the RANS simulation predicts a shock on the upper surface that occurs significantly upstream of the experimental shock.

The pressures on the surface predicted by the RANS simulations were interpolated onto a structured grid compatible with the SDPM. The panel vertices of this grid are given by

$$\begin{aligned}x_{p_i} &= c_0\left(1 - \sin\left(\frac{\pi}{2m}(i-1)\right)\right)\\ y_{p_j} &= \frac{b}{2}\cos\left(\pi - \frac{\pi}{n}(j-1)\right)\end{aligned}$$

for $i = 1,\ldots,2m+1$, $j = 1,\ldots,n+1$, where $2m$ is the number of panels in the chordwise direction (m on the lower and m on the upper

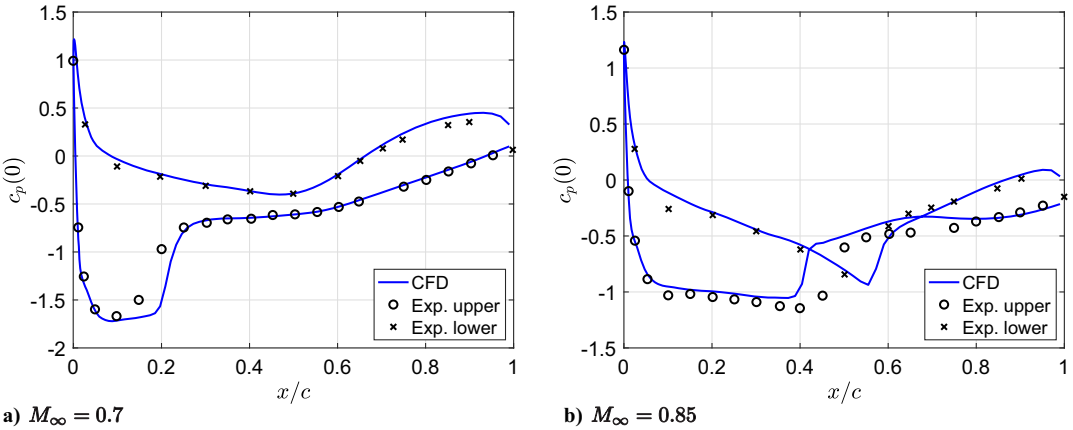

a) $M_\infty = 0.7$ b) $M_\infty = 0.85$

Fig. 1 Comparison of RANS and experimental pressure distributions for the BSCW wing at $\alpha = 5°$, $2y/b = 0.6$.

surface) and n is the number of panels in the spanwise direction. Consequently, $i = 1, \ldots, m$ denotes panels on the lower surface, and $i = m + 1, \ldots 2m$ denotes panels on the upper surface, for each spanwise station j. The computational fluid dynamics (CFD) grid was separated onto upper and lower surfaces using the camber line of the airfoil as separator. The pressures on each of the surfaces were then interpolated onto the SDPM grid. The derivative of the pressure distribution with respect to the pitch angle was calculated from

$$\boldsymbol{c}_{p_\alpha}^{\text{ref}} = \frac{\boldsymbol{c}_p^{\text{ref}}(5.5°) - \boldsymbol{c}_p^{\text{ref}}(4.5°)}{(5.5° - 4.5°)\pi/180°} \tag{41}$$

The SDPM corrections are based on $\boldsymbol{c}_{p_\alpha}^{\text{ref}}$, as calculated using the RANS pressure distributions and plotted in Fig. 2. There are no experimental measurements of $\boldsymbol{c}_{p_\alpha}$ to compare to, but some conclusions can be drawn from the figure. For $M_\infty = 0.7$, there is a very important negative peak in $\boldsymbol{c}_{p_\alpha}^{\text{ref}}$ at $x/c = 0.2$ that is due to the fact that the shock on the upper surface moves downstream as the angle of attack is increased. For $M_\infty = 0.85$, there is a very important and wide positive peak between $x/c = 0.4$ and $x/c = 0.6$ that is due to the fact that the shock on the upper surface moves upstream as the angle of attack is increased, albeit not uniformly over the span. There is also a less important negative peak on the lower surface, signifying that the shock on the lower surface moves slightly downstream with increasing angle of attack.

Figures 3a and 3b plot the oscillatory pressure distributions computed by the corrected SDPM and compare them to the uncorrected predictions and their experimental equivalents, for $\alpha = 5°, M_\infty = 0.7$,

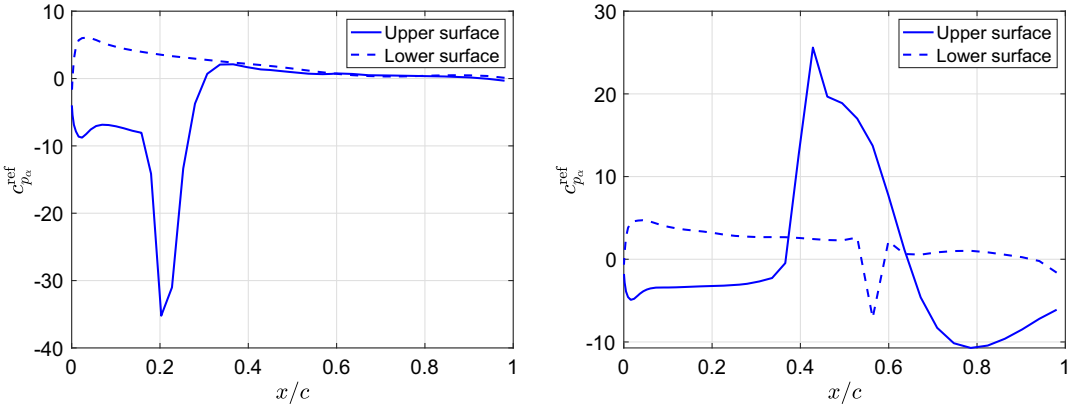

a) $M_\infty = 0.7$ **b)** $M_\infty = 0.85$

Fig. 2 Normalized reference pressure distribution at $2y/b = 0.6$, $\alpha_0 = 5°$ and two Mach number values.

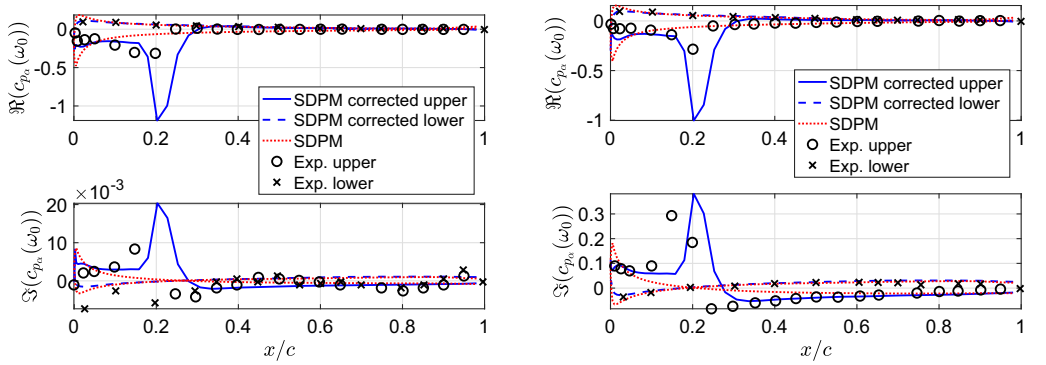

a) Oscillatory pressure distribution, $M_\infty = 0.7$, $k = 0.011$ **b) Oscillatory pressure distribution, $M_\infty = 0.7$, $k = 0.326$**

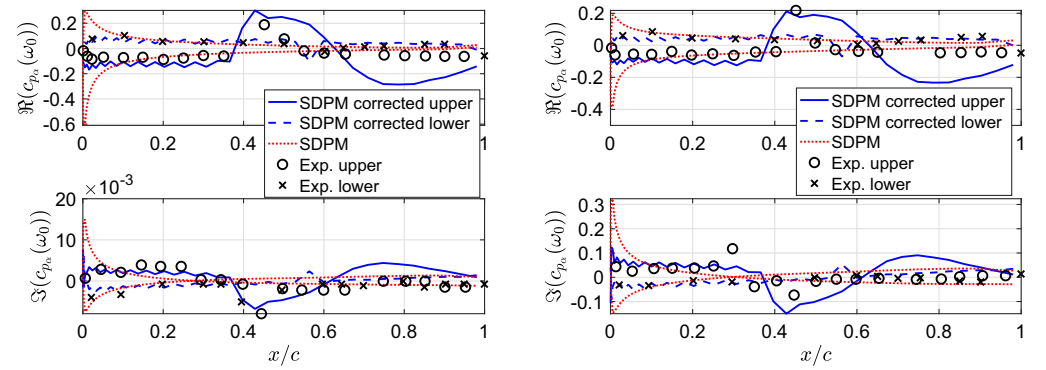

c) Oscillatory pressure distribution, $M_\infty = 0.85$, $k = 0.009$ **d) Oscillatory pressure distribution, $M_\infty = 0.85, k = 0.270$**

Fig. 3 Comparison of corrected SDPM and experimental pressure distributions at $\alpha_0 = 5°$, $2y/b = 0.6$.

and two values of the reduced frequency, $k = 0.011$ and $k = 0.326$. The amplitude of the real peak is higher than its experimental counterpart, but this inaccuracy is due to the negative peak in $\boldsymbol{c}_{p_\alpha}^{\text{ref}}$ seen in Fig. 2a. It should be stated that the experimental data plotted in Fig. 3 were read off from Fig. 14 of Piatak and Cleckner [14], so the imaginary values are not very accurate for the low reduced frequencies, due to their very low magnitude. It should also be noted that the peaks in the real and imaginary parts of the oscillatory pressure distribution predicted by the corrected SDPM occur downstream of the experimental peaks because the shock wave position was predicted downstream of the experimental shock by the RANS calculations. Nevertheless, the corrected pressure distributions are closer to the experimental data than the uncorrected SDPM results.

Figures 3c and 3d plot the oscillatory pressure distributions calculated by the corrected and uncorrected SDPM for $\alpha = 5°$, $M_\infty = 0.85$, and two values of the reduced frequency, $k = 0.009$ and $k = 0.270$, comparing them to the experimental measurements. At both reduced frequencies, the peak in the real part of the upper surface pressure distribution predicted by the corrected SDPM is wider than the experimental equivalent. This phenomenon is due to the width of the upper surface peak in $\boldsymbol{c}_{p_\alpha}^{\text{ref}}$ seen in Fig. 2b. Furthermore, both the real and imaginary parts demonstrate numerical oscillations upstream of the shock. This effect is due to noise in the $\boldsymbol{c}_{p_\alpha}^{\text{ref}}$ distribution, caused by the application of finite differences to two RANS solutions obtained at different angles of attack. Again, the corrected SDPM predictions lie closer to the experimental measurements than the uncorrected results.

VI. LANN Wing

The second application of the SDPM correction technique concerns the Lockheed-Georgia, U.S. Air Force Flight Dynamics Laboratory, NASA Langley, and Nationaal Lucht en Ruimtevaart Laboratorium (LANN) wing [15]. This half-wing model had an aspect ratio of 7.92, taper ratio of 0.4, leading-edge sweep of 27.493°, twist of −4.8°, root chord $c_0 = 0.3608$ m, half-span $b/2 = 1$ m, and half-area $S = 0.2526$ m^2. It featured a 12% thick supercritical airfoil whose ordinates at eight spanwise stations are given by Zwaan [15]. The pitch axis lay at $x_f = 0.224$ m behind the root leading edge. Steady and oscillatory pressure distributions were measured at six spanwise stations lying at $2y/b = 0.2, 0.325, 0.475, 0.65, 0.825$, and 0.95. Two test cases were selected from the LANN data set for the current analysis:

1) $M_\infty = 0.77, Re = 5.22 \times 10^6, \alpha_0 = 2.6°, \alpha_1 = 0.25°$, and $k = 0$ and 0.108.

2) $M_\infty = 0.82, Re = 5.43 \times 10^6, \alpha_0 = 0.6°, \alpha_1 = 0.25°$, and $k = 0$ and 0.051.

The fact that the wing was tested at $k = 0$ resulted in quasi-steady experimental estimates of $\boldsymbol{c}_{p_\alpha}^{\text{ref}}$ for both test cases.

Steady RANS simulations were carried out using the SU^2 [16] suite; for the $M_\infty = 0.77$ case, the chosen angles of attack were $\alpha_0 = 2.59°$, 2.60°, and 2.61°, while for $M_\infty = 0.82$, they were $\alpha_0 = 0.05°$, 0.06°, and 0.07°. The computational domain was a (half-)sphere, and its boundaries were placed at $50c_0$ away from the (half-)wing. The mesh was built using Gmsh [17]. The boundary-layer mesh was extruded from the surface grid and contained prismatic cells, while the rest of the domain was meshed using tetrahedral elements. The cell size on the body was between 0.5 and 1.0% of the local chord, and $y+$ was around 50. The mesh contained 7 million cells. The RANS equations with the Spalart–Allmaras turbulence model were discretized using the second-order Jameson–Schmidt–Turkel scheme. The boundary conditions were no-slip and wall functions on the body, symmetry on the symmetry plane, and far field based on Riemann invariants on the outer domain boundary. Additional calculations using the Spalart–Allmaras and the $k - \omega$ SST turbulence models were also performed on a wall-resolved grid. However, the results obtained using the Spalart–Allmaras model on the wall-modeled mesh were the closest to the experimental data. They have thus been retained for the present study. The reference values of $\boldsymbol{c}_{p_\alpha}^{\text{ref}}$ were calculated using finite difference schemes of the form of Eq. (41).

Figure 4 compares the RANS pressure distributions around the wing at the six spanwise measurement sections to the experimental data for $M_\infty = 0.77$ and $\alpha_0 = 2.60°$. The agreement between the two sets of results is generally good, except near the root where the shock predicted by the RANS simulation lies slightly downstream of the experimental shock wave. The experimental and simulated values of $\boldsymbol{c}_{p_\alpha}^{\text{ref}}$ are plotted in Fig. 5, again for the $M_\infty = 0.77$, $\alpha_0 = 2.6°$ case. Unlike the BSCW wing, the LANN wing was tested at $k = 0$, so the real part of the measured oscillatory pressure distribution is exactly equal to $\boldsymbol{c}_{p_\alpha}^{\text{ref}}$ and the imaginary part is exactly equal to zero. Figure 5 shows that there are significant differences in peak amplitudes between the RANS and experimental values of $\boldsymbol{c}_{p_\alpha}^{\text{ref}}$, at all spanwise stations. These differences may be due to unsteady effects that occurred during the experiment, despite the very low frequency, or to the finite difference calculation of $\boldsymbol{c}_{p_\alpha}^{\text{ref}}$ from the RANS simulation results.

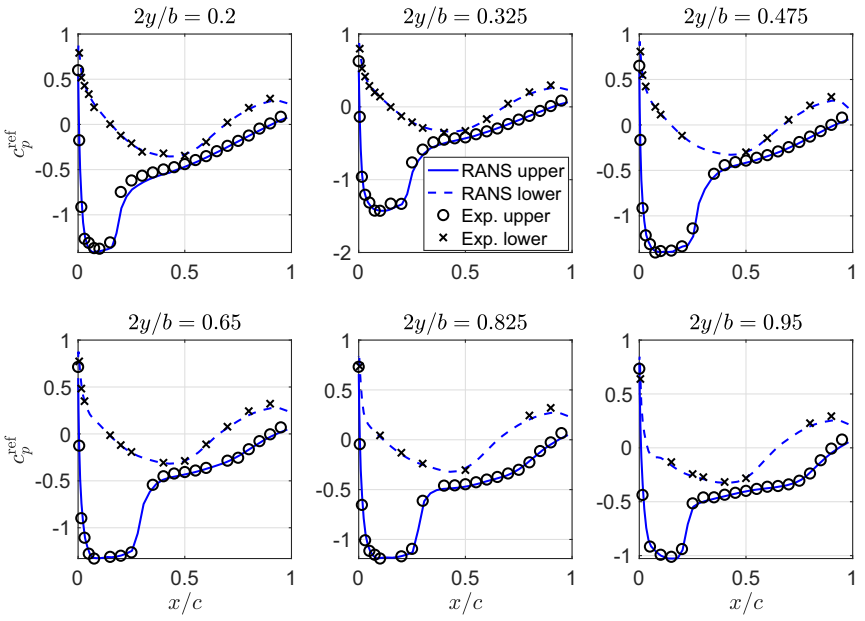

Fig. 4 Comparison of RANS and experimental pressure distributions for the LANN wing at $\alpha_0 = 2.6°$, $M_\infty = 0.77$.

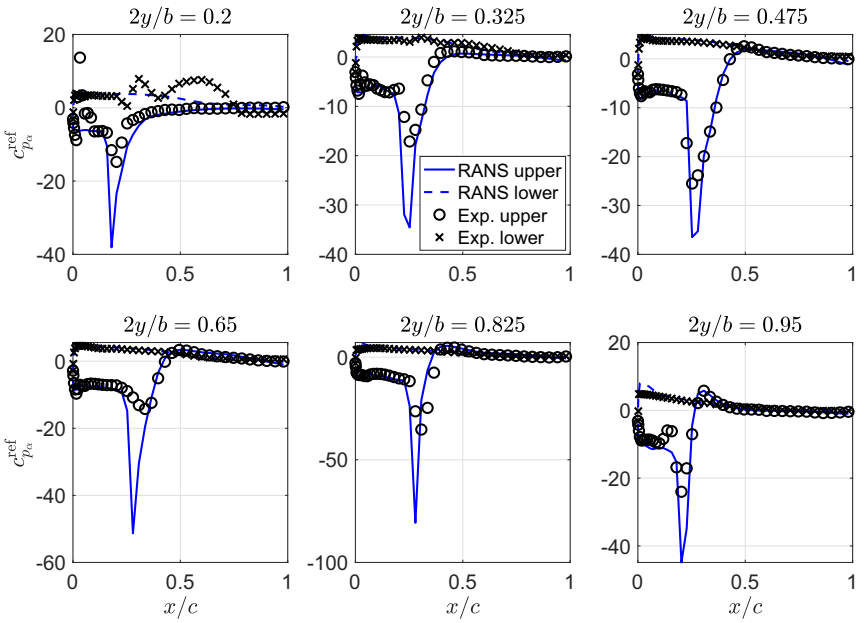

Fig. 5 Comparison of RANS and experimental $c_{p_\alpha}^{\text{ref}}$ distributions for the LANN wing at $\alpha_0 = 2.6°$, $M_\infty = 0.77$.

For the LANN wing, the SDPM corrections are also calculated from the experimental measurements of $\boldsymbol{c}_{p_\alpha}^{\text{ref}}$. There are only six spanwise measurement stations with up to 40 pressure taps each, so the experimental data must be extrapolated in order to calculate the reference pressures on the entire SDPM grid. This extrapolation is carried out by setting c_p to 1 at the trailing edge; at the wingtip, it is set to the values measured at $2y/b = 0.95$. There is no need to set a value for c_p at the leading edge because the interpolation is carried out using the chordwise arc length as an independent variable. The corrected oscillatory pressure distributions are then calculated as usual.

Figure 6 plots the real and imaginary parts of the oscillatory pressure distribution $c_{p_{\alpha_1}}(\omega_0) = 2ic_p(\omega_0)/\alpha_1$ for the case $M_\infty = 0.77$, $\alpha_0 = 2.6°$, $\alpha_1 = 0.25°$, and $k = 0.108$ at the six spanwise measurement stations. The SDPM corrections calculated using the CFD estimate for $\boldsymbol{c}_{p_\alpha}^{\text{ref}}$ are denoted by *SDPM CFD*, while those obtained from the experimental measurements of $\boldsymbol{c}_{p_\alpha}^{\text{ref}}$ are denoted by *SDPM Exp*. The predictions of the experimentally corrected SDPM lie significantly closer to the experimental results than the predictions of the CFD-based correction. In particular, the amplitudes of the peaks estimated using the CFD-based correction are consistently higher than those of the experimental distributions, due to the overestimation of the peak amplitudes in Fig. 5. The accuracy of the SDPM correction obtained from the experimental value of $\boldsymbol{c}_{p_\alpha}^{\text{ref}}$ shows that the correction technique presented here is sound but the data used to calculate this correction must be adequate. Note that neither of the corrections can predict accurately the imaginary part of the pressure distribution near the wingtip ($2y/b = 0.95$).

Figure 7 plots the unsteady pressure distributions obtained by the corrected SDPM technique for the test case $M_\infty = 0.82$, $\alpha_0 = 0.6°$, $\alpha_1 = 0.25°$, and $k = 0.051$. Corrections obtained both using experimental and CFD $\boldsymbol{c}_{p_\alpha}^{\text{ref}}$ distributions are plotted, along with the experimental measurements. Once more, the corrections obtained using

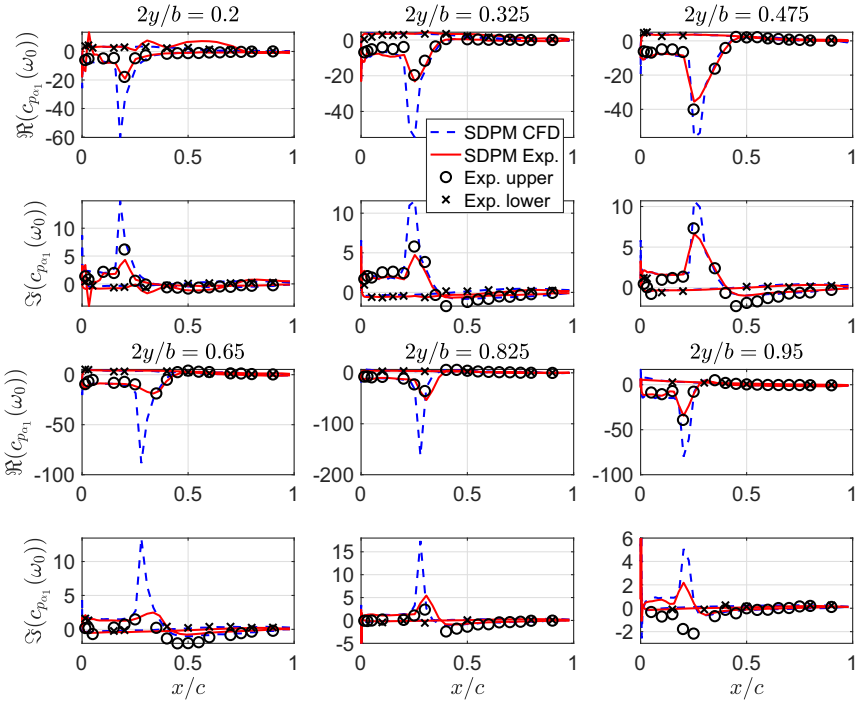

Fig. 6 Corrected oscillatory pressure distributions at $\alpha_0 = 2.6°$, $k = 0.10$, $M_\infty = 0.77$.

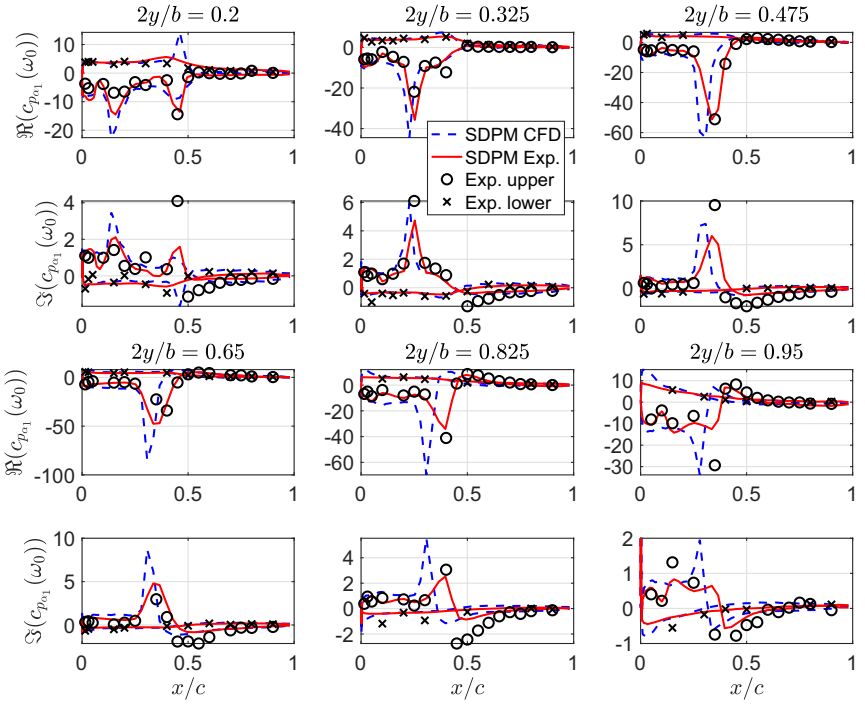

Fig. 7 Corrected oscillatory pressure distributions at $\alpha_0 = 0.6°$, $k = 0.05$, $M_\infty = 0.82$.

the experimental value of $\boldsymbol{c}_{p_\alpha}^{\text{ref}}$ lie closer to the experimental oscillatory pressure distributions. In this case, the amplitudes of the peaks of the correction calculated using the CFD data are less overestimated than in the $M_\infty = 0.77$ case, but their locations lie systematically upstream of the experimentally measured peaks.

VII. Flutter Predictions for the AGARD Wing

In this section, the SDPM with transonic correction is applied to the weakened AGARD 445.6 wing test case [18]. This experimental test case consisted of a flexible half-wing model with root chord $c_0 = 0.589$ m, taper ratio $\lambda = 0.6576$, half-span $b/2 = 0.762$ m, sweep angle at the quarter-chord $\Lambda_{c/4} = 45°$, half-aspect-ratio 1.6525, and a NACA 65A004 airfoil section oriented in the streamwise direction. It was installed at an angle $\alpha_0 = 0°$ in the Langley Transonic Dynamics Tunnel and tested for flutter using both air and freon as the testing medium. The freestream Mach numbers of the tests ranged from 0.34 to 1.14.

The finite element model for this wing was created using the Equivalent Plate Method [19,20]. The first $M = 5$ modes extracted using this model were in good agreement with the modal parameters and shapes published in the literature [18]. The application of the uncorrected SDPM approach to modal models of wings is described in detail in Ref. [21]. Pressure derivatives are calculated with respect to the degrees of freedom of the finite element model such that

$$\begin{aligned}\boldsymbol{c}_p(k_0) = &(\boldsymbol{c}_{p_\phi}(k_0) + \boldsymbol{c}_{p_\theta}(k_0))\boldsymbol{q}(k_0)\\ &+ \mathrm{i}k_0(\boldsymbol{c}_{p_{\bar{z}}}(k_0) + \boldsymbol{c}_{p_{\dot{\phi}}}(k_0) + \boldsymbol{c}_{p_{\dot{\theta}}}(k_0))\boldsymbol{q}(k_0)\\ &+ (\mathrm{i}k_0)^2\boldsymbol{c}_{p_{\ddot{z}}}(k_0)\boldsymbol{q}(k_0)\end{aligned} \tag{42}$$

where $\boldsymbol{q}(k_0)$ are generalized coordinates,

$$\begin{aligned}\boldsymbol{c}_{p_\theta}(k_0) &= -\bar{\boldsymbol{C}}_0(k_0)(\tilde{\boldsymbol{\Phi}}_\theta \circ \boldsymbol{n}_\zeta) - 2\bar{\boldsymbol{w}}(0) \circ \tilde{\boldsymbol{\Phi}}_\theta\\ \boldsymbol{c}_{p_{\bar{z}}}(k_0) &= -\frac{2}{c_0}(\bar{\boldsymbol{C}}_0(k_0)(\tilde{\boldsymbol{\Phi}}_z \circ \boldsymbol{n}_\zeta) + 2\bar{\boldsymbol{w}}(0) \circ \tilde{\boldsymbol{\Phi}}_z)\\ \boldsymbol{c}_{p_{\dot{\theta}}}(k_0) &= -\frac{2}{c_0}\bar{\boldsymbol{C}}_1(k_0)(\tilde{\boldsymbol{\Phi}}_\theta \circ \boldsymbol{n}_\zeta)\\ \boldsymbol{c}_{p_{\ddot{z}}}(k_0) &= -\frac{4}{c_0^2}\bar{\boldsymbol{C}}_1(k_0)(\tilde{\boldsymbol{\Phi}}_z \circ \boldsymbol{n}_\zeta)\end{aligned}$$

$\tilde{\boldsymbol{\Phi}}_\theta$ and $\tilde{\boldsymbol{\Phi}}_z$ are $N \times M$ mode shape matrices in out-of plane bending and torsion; and $\bar{\boldsymbol{C}}_0$ and $\bar{\boldsymbol{C}}_1(k_0)$ are normalized versions of matrices $\boldsymbol{C}_0(\omega_0)$ and $\boldsymbol{C}_1(\omega_0)$, such that

$$\begin{aligned}\bar{\boldsymbol{C}}_0(k_0) = &2M_\infty^2\boldsymbol{K}_x(k_0) \circ \bar{\boldsymbol{\phi}}_x(0) - 2\boldsymbol{K}_x(k_0) \circ \bar{\boldsymbol{u}}(0) - 2\boldsymbol{K}_y(k_0) \circ \bar{\boldsymbol{v}}(0)\\ &- 2\boldsymbol{K}_z(k_0) \circ \bar{\boldsymbol{w}}(0)\\ \bar{\boldsymbol{C}}_1(k_0) = &2\,\boldsymbol{K}(k_0) - 2M_\infty^2\boldsymbol{K}(k_0) \circ \bar{\boldsymbol{\phi}}_x(0)\end{aligned} \tag{43}$$

noting that $\bar{\boldsymbol{u}}(0) = \boldsymbol{u}(0)/U_\infty$, $\bar{\boldsymbol{v}}(0) = \boldsymbol{v}(0)/U_\infty$, $\bar{\boldsymbol{w}}(0) = \boldsymbol{w}(0)/U_\infty$, and $\bar{\boldsymbol{\phi}}_x(0) = \boldsymbol{\phi}_x(0)/U_\infty$. The aeroelastic equation of motion is

$$\boldsymbol{A}\ddot{\boldsymbol{q}} + \boldsymbol{C}\dot{\boldsymbol{q}} + \boldsymbol{E}\boldsymbol{q} = \frac{1}{2}\rho Q_\infty^2(\boldsymbol{Q}_0(k_0) + \mathrm{i}k_0\boldsymbol{Q}_1(k_0) + (\mathrm{i}k_0)^2\boldsymbol{Q}_2(k_0))\boldsymbol{q} \tag{44}$$

where $\boldsymbol{A}$, $\boldsymbol{C}$, and $\boldsymbol{E}$ are the structural mass, damping, and stiffness matrices, while $\boldsymbol{Q}_0(k_0)$, $\boldsymbol{Q}_1(k_0)$, and $\boldsymbol{Q}_2(k_0)$ are generalized aerodynamic force matrices given by

$$\begin{aligned}\boldsymbol{Q}_0(k_0) &= \tilde{\boldsymbol{\Phi}}_\theta^T(\boldsymbol{c}_{p_\theta}(k_0) \circ \boldsymbol{s} \circ \boldsymbol{n}_z)\\ \boldsymbol{Q}_1(k_0) &= \tilde{\boldsymbol{\Phi}}_z^T(\boldsymbol{c}_{p_{\bar{z}}}(k_0) \circ \boldsymbol{s} \circ \boldsymbol{n}_z) + \tilde{\boldsymbol{\Phi}}_\theta^T(\boldsymbol{c}_{p_{\dot{\theta}}}(k_0) \circ \boldsymbol{s} \circ \boldsymbol{n}_z)\\ \boldsymbol{Q}_2(k_0) &= \tilde{\boldsymbol{\Phi}}_z^T(\boldsymbol{c}_{p_{\ddot{z}}}(k_0) \circ \boldsymbol{s} \circ \boldsymbol{n}_z)\end{aligned} \tag{45}$$

The structural damping matrix can be represented using the complex proportional stiffness model, such that $\boldsymbol{C}\dot{\boldsymbol{q}} + \boldsymbol{E}\boldsymbol{q}$ transforms to $(1 + \mathrm{i}g)\boldsymbol{E}\boldsymbol{q}(\omega)$ in the frequency domain, where $g = 0.02$ is the value recommended for the structural damping coefficient [18]. Equation (44) is solved for the system eigenvalues using the determinant iteration technique.

The steady pressure distributions used to estimate the transonic correction were obtained using three approaches:

1) A solution of the Full Potential Equation (FPE) using the DART software [22].[‡‡] The half-wing was placed in a rectangular box whose boundaries extended 20 chords away from the wing's surface. The unstructured tetrahedral mesh was built using Gmsh. The cell size on the wing surface was between 0.5 and 1.0% of the local chord, and a

[‡‡]Data available online at https://gitlab.uliege.be/am-dept/dartflo [retrieved 1 March 2024].

stretching ratio of 1.1 was imposed on the size of the volume cells, resulting in a mesh of 540,000 cells. A zero normal flux boundary condition was enforced on the body, and the normal flux was imposed to its freestream value on the outer domain boundaries. Additionally, the Kutta condition was imposed between the wing's trailing edge and the wake, and a symmetry boundary condition was used on the symmetry plane. The full potential equation was solved using a quasi-Newton algorithm with line search.

2) A solution of the Euler equations using SU^2. The half-wing was placed inside a half-sphere whose boundaries extended 50 chords away from the wing surface. As in the case of DART, the unstructured grid was built using Gmsh. The unstructured mesh contained 410,000 cells, which is lower than the number of cells used for DART. Full potential solvers require a wake model, resulting in cell clustering. The Euler equations were discretized using the second-order Jameson–Schmidt–Turkel scheme. The boundary conditions were slip wall on the wing, symmetry on the symmetry plane, and far field based on Riemann invariants on the outer domain boundaries.

3) A solution of the RANS equations using SU^2. The same computational domain was used for the Euler and RANS computations. The unstructured grid was built using Gmsh, as for the Euler and full potential solvers, with the addition that the boundary-layer mesh was extruded from the surface grid and contained prismatic cells. The boundary layer was resolved up to $y+ = 1$, and the mesh contained 3.5 million cells. The RANS equations with the Spalart–Allmaras turbulence model were discretized using the second-order Jameson–Schmidt–Turkel scheme. The boundary conditions were no-slip wall on the wing, symmetry on the symmetry plane, and far field based on Riemann invariants on the outer domain boundary.

Steady simulations were carried out at two Mach numbers, $M_\infty = 0.9$ and $M_\infty = 0.96$, as well as at two angles of attack, $\alpha = -0.1°$ and $\alpha = 0.1°$. Then, for both Mach numbers, the steady reference pressure derivatives around $\alpha = 0°$ can be estimated from

$$\boldsymbol{c}_{p_\alpha}^{\text{ref}} = \frac{\boldsymbol{c}_p(0.1°) - \boldsymbol{c}_p(-0.1°)}{0.2°\pi/180°}$$

The correction is then evaluated using Eqs. (33) and (36), and the normalized version of Eq. (38)

$$\begin{aligned}\bar{\boldsymbol{C}}_0^{\text{corr}}(k_0) &= 2M_\infty^2 \boldsymbol{K}_x^{\text{corr}}(k_0) \circ \bar{\boldsymbol{\phi}}_x^{\text{corr}}(0) - 2\boldsymbol{K}_x^{\text{corr}}(k_0) \circ \bar{\boldsymbol{u}}^{\text{corr}}(0) \\ &\quad - 2\boldsymbol{K}_y^{\text{corr}}(k_0) \circ \bar{\boldsymbol{v}}^{\text{corr}}(0) - 2\boldsymbol{K}_z^{\text{corr}}(k_0) \circ \bar{\boldsymbol{w}}^{\text{corr}}(0) \\ \bar{\boldsymbol{C}}_1^{\text{corr}}(k_0) &= 2\boldsymbol{K}^{\text{corr}}(k_0) - 2M_\infty^2 \boldsymbol{K}^{\text{corr}}(k_0) \circ \bar{\boldsymbol{\phi}}_x^{\text{corr}}(0)\end{aligned} \tag{46}$$

The corrected pressure derivatives are calculated from

$$\begin{aligned}\boldsymbol{c}_{p_\theta}^{\text{corr}}(k_0) &= -\bar{\boldsymbol{C}}_0^{\text{corr}}(k_0)(\tilde{\boldsymbol{\Phi}}_\theta \circ \boldsymbol{n}_\zeta) - 2\bar{\boldsymbol{w}}^{\text{corr}}(0) \circ \tilde{\boldsymbol{\Phi}}_\theta \\ \boldsymbol{c}_{p_{\dot{z}}}^{\text{corr}}(k_0) &= -\frac{2}{c_0}(\bar{\boldsymbol{C}}_0^{\text{corr}}(k_0)(\tilde{\boldsymbol{\Phi}}_z \circ \boldsymbol{n}_\zeta) + 2\bar{\boldsymbol{w}}^{\text{corr}}(0) \circ \tilde{\boldsymbol{\Phi}}_z) \\ \boldsymbol{c}_{p_{\dot{\theta}}}^{\text{corr}}(k_0) &= -\frac{2}{c_0}\bar{\boldsymbol{C}}_1^{\text{corr}}(k_0)(\tilde{\boldsymbol{\Phi}}_\theta \circ \boldsymbol{n}_\zeta) \\ \boldsymbol{c}_{p_{\ddot{z}}}^{\text{corr}}(k_0) &= -\frac{4}{c_0^2}\bar{\boldsymbol{C}}_1^{\text{corr}}(k_0)(\tilde{\boldsymbol{\Phi}}_z \circ \boldsymbol{n}_\zeta)\end{aligned}$$

and substituted in Eq. (46) to obtain the corrected generalized aerodynamic force matrices.

Figure 8 plots the variation of the flutter speed Q_F and frequency ω_F with freestream Mach number for the AGARD wing. The uncorrected SDPM predictions are denoted by *SDPM*, the corrections obtained using RANS simulations are denoted by *RANS corr*, those obtained using the Euler solver are denoted by *Euler corr*, those obtained using the full potential solver are denoted by *FPE corr*, while the experimental measurements are denoted by *Exp*. It can be seen that the uncorrected SDPM predictions for the flutter speed are acceptable up to $M_\infty = 0.9$ but increase discontinuously at $M_\infty = 0.96$. The corresponding flutter frequency predictions are overestimated at $M_\infty = 0.5$ and $M_\infty = 0.68$ but lie close to the experimental measurements at higher Mach numbers. The AGARD 445.6 wing features a very thin airfoil, and shock waves occur on its surface at Mach numbers higher than 0.9 [23], which explains the good performance of the uncorrected SDPM for Mach numbers up to $M_\infty = 0.9$. The transonic flutter dip of this wing is not very pronounced, it is usually extrapolated from the overprediction of the flutter speed by linear methods at $M_\infty = 0.96$.

The corrected SDPM results were obtained only for $M_\infty = 0.9$ and $M_\infty = 0.96$. It is clear that the corrected flutter speed and frequency estimates, as obtained from all three values of $\boldsymbol{c}_{p_\alpha}^{\text{ref}}$, lie closer to the wind-tunnel data than the uncorrected predictions. Figure 9 plots the same data in nondimensional form. The flutter speed index is defined as

$$Q_F^* = \frac{2Q_F}{c_0\omega_\alpha\sqrt{\mu}}$$

where ω_α is the frequency of the first torsion mode, as calculated from the finite element (FE) model, and μ is the experimental value of the mass ratio. It can be seen that the corrected SDPM estimates of Q_F^* undergo a more abrupt drop at $M_\infty = 0.96$ than the uncorrected ones.

VIII. Conclusions

A new method has been presented for the correction of the unsteady pressure distributions predicted by the source and doublet panel method under transonic flow conditions. The approach is based on correcting the terms relative to the upwash velocity appearing in

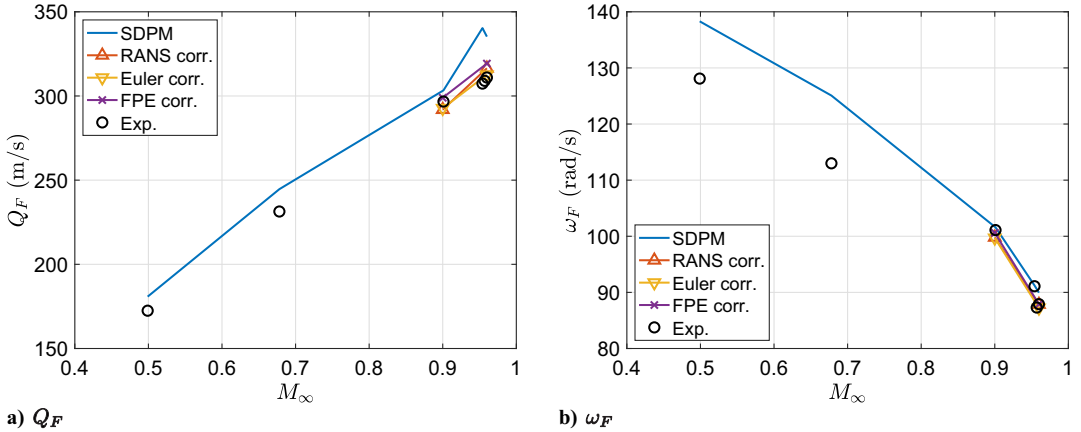

a) Q_F b) ω_F

Fig. 8 Flutter speeds and frequencies calculated for the AGARD wing by the SDPM with three corrections, compared to experimental measurements.

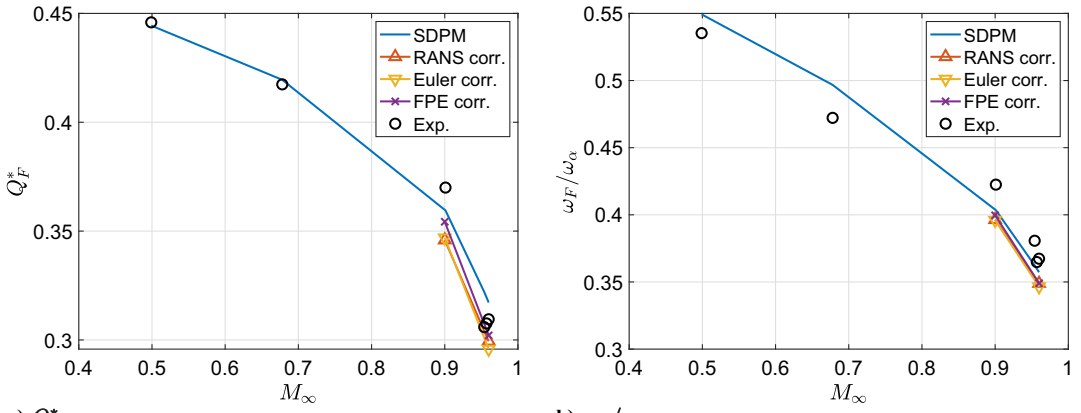

a) Q_F^* b) ω_F/ω_α

Fig. 9 Flutter indices and frequency ratios calculated for the AGARD wing by the SDPM with three corrections, compared to experimental measurements.

the equations of the pressure derivatives using a reference distribution of the normalized pressure coefficient $\boldsymbol{c}_{p_\alpha}^{\text{ref}}$. Even though the correction matrix $\boldsymbol{D}_{\text{corr}}$ is calculated after linearizing the steady pressure coefficient equation of the SDPM, the equation for the oscillating pressure distribution $\boldsymbol{c}_p(\omega)$ does not need to be linearized, and it remains a second-order approximation of the unsteady compressible Bernoulli equation. No correction is necessary for the mean pressure distribution $\boldsymbol{c}_p(0)$ because the reference pressure distribution can be used instead. The second harmonic of the pressure $\boldsymbol{c}_p(2\omega)$ has not been corrected because it is usually not required. Such a correction could be necessary in the context of a nonlinear aeroelastic computation carried out by means of the Harmonic Balance method but is left as future work.

Applications of the SDPM correction methodology to two pitching oscillation test cases from the literature show that its predictions are accurate as long as the values used for $\boldsymbol{c}_{p_\alpha}^{\text{ref}}$ are adequate. The best predictions were obtained when using experimentally measured $\boldsymbol{c}_{p_\alpha}^{\text{ref}}$ distributions. Corrections calculated using RANS simulation results can suffer from two problems: the steady RANS predictions may not match exactly the position and strength of the shock wave(s), and the calculation of $\boldsymbol{c}_{p_\alpha}^{\text{ref}}$ using numerical differentiation can lead to overestimated peak amplitudes and noise. Nevertheless, an application of the present correction methodology to the flutter prediction of the AGARD wing has shown that these problems have minor effects on the resulting flutter speeds and frequencies. Corrections calculated from three different sets of steady solutions (RANS, Euler, and full potential) yielded very similar flutter predictions at transonic conditions.

Corrections to linear methods calculated using steady higher-fidelity models or experimental data can represent not only transonic effects, such as shock waves, but also viscous effects, such as viscous decambering and mild flow separation. The development of the present correction technique means that the SDPM could now be considered as a fully featured alternative to the Doublet Lattice Method. Even though the two approaches are solutions of the same flow equation, the SDPM can output more information because it can calculate and correct steady and unsteady pressure distributions around the exact geometry of the wing or body being studied.

Appendix: Terms in Eqs. (21) and (25)

This Appendix gives expressions for the various terms in Eqs. (21) and (25). If $\boldsymbol{\xi}_c$, $\boldsymbol{\eta}_c$, and $\boldsymbol{\zeta}_c$ are $N \times 1$ vectors whose elements are the Prandtl–Glauert coordinates of the panel control points, then the distance between the Ith and Jth control points is given by

$$r(\boldsymbol{\xi}_{c_I}, \boldsymbol{\xi}_{c_J}) = \sqrt{(\xi_{c_I} - \xi_{c_J})^2 + (\eta_{c_I} - \eta_{c_J})^2 + (\zeta_{c_I} - \zeta_{c_J})^2}$$

The elements of matrices $\bar{\boldsymbol{A}}(\omega)$, $\bar{\boldsymbol{B}}_\phi(\omega)$, and $\bar{\boldsymbol{C}}_\phi(\omega)$ in Eq. (21) are obtained from [8,11]

$$\bar{A}_{\phi_{IJ}}(\omega) = \mathrm{e}^{-\mathrm{i}\Omega(-M_\infty(\xi_{c_I}-\xi_{c_J})+r(\boldsymbol{\xi}_{c_I},\boldsymbol{\xi}_{c_J}))} A_{\phi_{IJ}}$$
$$\bar{B}_{\phi_{IJ}}(\omega) = -\mathrm{i}\Omega \mathrm{e}^{-\mathrm{i}\Omega(-M_\infty(\xi_{c_I}-\xi_{c_J})+r(\boldsymbol{\xi}_{c_I},\boldsymbol{\xi}_{c_J}))} M_\infty n_\xi(\boldsymbol{\xi}_{c_J}) A_{\phi_{IJ}} + (1 + \mathrm{i}\Omega r(\boldsymbol{\xi}_{c_I}, \boldsymbol{\xi}_{c_J}))\mathrm{e}^{-\mathrm{i}\Omega(-M_\infty(\xi_{c_I}-\xi_{c_J})+r(\boldsymbol{\xi}_{c_I},\boldsymbol{\xi}_{c_J}))} B_{\phi_{IJ}}$$

for $I = 1, \ldots, N$, $J = 1, \ldots, N$ and

$$\bar{C}_{\phi_{IJ}}(\omega) = (1 + \mathrm{i}\Omega r(\boldsymbol{\xi}_{c_I}, \boldsymbol{\xi}_{c_J}))\mathrm{e}^{-\mathrm{i}\Omega(-M_\infty(\xi_{c_I}-\xi_{c_J})+r(\boldsymbol{\xi}_{c_I},\boldsymbol{\xi}_{c_J}))} C_{\phi_{IJ}}$$

for $I = 1, \ldots, N$, $J = 1, \ldots, N_w$. In these last three expressions, the matrices $\boldsymbol{A}_\phi$, $\boldsymbol{B}_\phi$, and $\boldsymbol{C}_\phi$ are those obtained for steady subsonic flow, for example, using the approach by Hess and Smith [24] or, equivalently, the expressions given by Katz and Plotkin [25] or Dimitriadis [8]. Note that $B_{\phi_{II}} = 0$. Furthermore, if the wake is discretized into m_w chordwise and n spanwise panels, then

$$\boldsymbol{P}_c = (\boldsymbol{0}_{n\times(2m-1)n}\boldsymbol{I}_n) - (\boldsymbol{I}_n\boldsymbol{0}_{n\times(2m-1)n})$$
$$\boldsymbol{P}_e(\omega) = \begin{pmatrix} \boldsymbol{I}_n \mathrm{e}^{-\mathrm{i}\omega\Delta t} \\ \boldsymbol{I}_n \mathrm{e}^{-\mathrm{i}\omega 2\Delta t} \\ \vdots \\ \boldsymbol{I}_n \mathrm{e}^{-\mathrm{i}\omega m_w \Delta t} \end{pmatrix}$$

where the time step is chosen as $\Delta t = c_0/mQ_\infty$. The terms $\boldsymbol{a}_1$, $\boldsymbol{a}_2$, $\boldsymbol{b}_1$, $\boldsymbol{b}_2$, $\boldsymbol{c}_1$, $\boldsymbol{c}_2$, $\boldsymbol{D}^m$, $\boldsymbol{D}^n$, $\Delta\boldsymbol{s}_m$, and $\Delta\boldsymbol{s}_n$ in Eq. (25) are given by [12,13]

$$\Delta\boldsymbol{\xi}_c = \boldsymbol{D}^m\boldsymbol{\xi}_c, \ \Delta\boldsymbol{\eta}_c = \boldsymbol{D}^m\boldsymbol{\eta}_c, \ \Delta\boldsymbol{\zeta}_c = \boldsymbol{D}^m\boldsymbol{\zeta}_c$$
$$\Delta\boldsymbol{\mu} = \boldsymbol{D}^m\boldsymbol{\mu}, \ \Delta\boldsymbol{s}_m = \sqrt{\Delta\boldsymbol{\xi}_c \circ \Delta\boldsymbol{\xi}_c + \Delta\boldsymbol{\eta}_c \circ \Delta\boldsymbol{\eta}_c + \Delta\boldsymbol{\zeta}_c \circ \Delta\boldsymbol{\zeta}_c}$$
$$\boldsymbol{\tau}_{m_\xi} = \Delta\boldsymbol{\xi}_c \oslash \Delta\boldsymbol{s}_m, \ \boldsymbol{\tau}_{m_\eta} = \Delta\boldsymbol{\eta}_c \oslash \Delta\boldsymbol{s}_m, \ \boldsymbol{\tau}_{m_\zeta} = \Delta\boldsymbol{\zeta}_c \oslash \Delta\boldsymbol{s}_m$$

$$D^m_{i,i} = -1, \text{ for } i = 1, \ldots, n$$
$$D^m_{i,n+i} = 1, \text{ for } i = 1, \ldots, n$$
$$D^m_{(2m-1)n+i,(2m-2)n+i} = -1, \text{ for } i = 1, \ldots, n$$
$$D^m_{(2m-1)n+i,(2m-1)n+i} = 1, \text{ for } i = 1, \ldots, n$$
$$D^m_{n+i,i} = -1, \text{ for } i = 1, \ldots, 2(m-2)n$$
$$D^m_{n+i,2n+i} = 1, \text{ for } i = 1, \ldots, 2(m-2)n$$

$$\Delta\boldsymbol{\xi}_c = \boldsymbol{D}^n\boldsymbol{\xi}_c, \ \Delta\boldsymbol{\eta}_c = \boldsymbol{D}^n\boldsymbol{\eta}_c, \ \Delta\boldsymbol{\zeta}_c = \boldsymbol{D}^n\boldsymbol{\zeta}_c$$
$$\Delta\boldsymbol{\mu} = \boldsymbol{D}^n\boldsymbol{\mu}, \ \Delta\boldsymbol{s}_n = \sqrt{\Delta\boldsymbol{\xi}_c \circ \Delta\boldsymbol{\xi}_c + \Delta\boldsymbol{\eta}_c \circ \Delta\boldsymbol{\eta}_c + \Delta\boldsymbol{\zeta}_c \circ \Delta\boldsymbol{\zeta}_c}$$
$$\boldsymbol{\tau}_{n_\xi} = \Delta\boldsymbol{\xi}_c \oslash \Delta\boldsymbol{s}_n, \ \boldsymbol{\tau}_{n_\eta} = \Delta\boldsymbol{\eta}_c \oslash \Delta\boldsymbol{s}_n, \ \boldsymbol{\tau}_{n_\zeta} = \Delta\boldsymbol{\zeta}_c \oslash \Delta\boldsymbol{s}_n$$

$$
\begin{aligned}
D^n_{1+(i-1)n,1+(i-1)n} &= -1, \text{ for } i = 1,\ldots,2m\\
D^n_{1+(i-1)n,2+(i-1)n} &= 1, \text{ for } i = 1,\ldots,2m\\
D^n_{in,in-1} &= -1, \text{ for } i = 1,\ldots,2m\\
D^n_{in,in} &= 1, \text{ for } i = 1,\ldots,2m\\
D^n_{(i-1)n+j,(i-1)n+j-1} &= -1, \text{ for } i = 1,\ldots,2m \text{ and } j = 2,\ldots,n-1\\
D^n_{(i-1)n+j,(i-1)n+j+1} &= 1, \text{ for } i = 1,\ldots,2m \text{ and } j = 2,\ldots,n-1
\end{aligned}
$$

$$
\begin{aligned}
\boldsymbol{d} &= \boldsymbol{n}_\xi \circ \boldsymbol{\tau}_{m_\eta} \circ \boldsymbol{\tau}_{n_\zeta} - \boldsymbol{n}_\xi \circ \boldsymbol{\tau}_{m_\zeta} \circ \boldsymbol{\tau}_{n_\eta} - \boldsymbol{n}_\eta \circ \boldsymbol{\tau}_{m_\xi} \circ \boldsymbol{\tau}_{n_\zeta}\\
&\quad + \boldsymbol{n}_\eta \circ \boldsymbol{\tau}_{m_\zeta} \circ \boldsymbol{\tau}_{n_\xi} + \boldsymbol{n}_\zeta \circ \boldsymbol{\tau}_{m_\xi} \circ \boldsymbol{\tau}_{n_\eta} - \boldsymbol{n}_\zeta \circ \boldsymbol{\tau}_{m_\eta} \circ \boldsymbol{\tau}_{n_\xi}\\
\boldsymbol{a}_1 &= -(\boldsymbol{n}_\eta \boldsymbol{\tau}_{n_\zeta} - \boldsymbol{n}_\zeta \boldsymbol{\tau}_{n_\eta}) \oslash \boldsymbol{d}\\
\boldsymbol{a}_2 &= (\boldsymbol{n}_\eta \boldsymbol{\tau}_{m_\zeta} - \boldsymbol{n}_\zeta \boldsymbol{\tau}_{m_\eta}) \oslash \boldsymbol{d}\\
\boldsymbol{a}_3 &= (\boldsymbol{\tau}_{m_\eta} \boldsymbol{\tau}_{n_\zeta} - \boldsymbol{m}_\zeta \boldsymbol{\tau}_{n_\eta}) \oslash \boldsymbol{d}\\
\boldsymbol{b}_1 &= -(\boldsymbol{n}_\xi \boldsymbol{\tau}_{n_\zeta} - \boldsymbol{n}_\zeta \boldsymbol{\tau}_{n_\xi}) \oslash \boldsymbol{d}\\
\boldsymbol{b}_2 &= (\boldsymbol{n}_\xi \boldsymbol{\tau}_{m_\zeta} - \boldsymbol{n}_\zeta \boldsymbol{\tau}_{m_\xi}) \oslash \boldsymbol{d}\\
\boldsymbol{b}_3 &= (\boldsymbol{\tau}_{m_\xi} \boldsymbol{\tau}_{n_\zeta} - \boldsymbol{m}_\zeta \boldsymbol{\tau}_{n_\xi}) \oslash \boldsymbol{d}\\
\boldsymbol{c}_1 &= -(\boldsymbol{n}_\xi \boldsymbol{\tau}_{n_\eta} - \boldsymbol{n}_\eta \boldsymbol{\tau}_{n_\xi}) \oslash \boldsymbol{d}\\
\boldsymbol{c}_2 &= (\boldsymbol{n}_\xi \boldsymbol{\tau}_{m_\eta} - \boldsymbol{n}_\eta \boldsymbol{\tau}_{m_\xi}) \oslash \boldsymbol{d}\\
\boldsymbol{c}_3 &= (\boldsymbol{\tau}_{m_\xi} \boldsymbol{\tau}_{n_\eta} - \boldsymbol{m}_\eta \boldsymbol{\tau}_{n_\xi}) \oslash \boldsymbol{d}
\end{aligned}
$$

References

[1] Albano, E., and Rodden, W. P., "A Doublet-Lattice Method for Calculating Lift Distributions on Oscillating Surfaces in Subsonic Flows," *AIAA Journal*, Vol. 7, No. 2, 1969, pp. 279–285. https://doi.org/10.2514/3.5086

[2] Kalman, T. P., Rodden, W. P., and Giesing, J. P., "Application of the Doublet Lattice Method to Nonplanar Configurations in Subsonic Flow," *AIAA Journal*, Vol. 8, No. 6, 1971, pp. 406–413. https://doi.org/10.2514/3.59117

[3] Giesing, J. P., Kalman, T. P., and Rodden, W. P., "Correction Factor Techniques for Improving Aerodynamic Prediction Methods," NASA CR 144967, 1976.

[4] Palacios, R., Climent, H., Karlsson, A., and Winzell, B., "Assessment of Strategies for Correcting Linear Unsteady Aerodynamics Using CFD or Test Results," *International Forum on Aeroelasticity and Structural Dynamics*, Paper IFASD2001-074, Madrid, Spain, June 2017.

[5] Silva, R. G. A., Mello, O. A. F., Azevedo, J. L. F., Chen, P. C., and Liu, D. D., "Investigation on Transonic Correction Methods for Unsteady Aerodynamics and Aeroelastic Analyses," *Journal of Aircraft*, Vol. 45, No. 6, 2008, pp. 1890–1903. https://doi.org/10.2514/1.33406

[6] Morino, L., "A General Theory of Unsteady Compressible Potential Aerodynamics," NASA CR-2464, 1974.

[7] Morino, L., Chen, L., and Suciu, E. O., "Steady and Oscillatory Subsonic and Supersonic Aerodynamics Around Complex Configurations," *AIAA Journal*, Vol. 13, No. 3, 1975, pp. 368–374. https://doi.org/10.2514/3.49706

[8] Dimitriadis, G., *Unsteady Aerodynamics—Potential and Vortex Methods*, Wiley, Hoboken, NJ, 2023. https://doi.org/10.1002/9781119762560

[9] Friedewald, D., Thormann, R., Kaiser, C., and Nitzsche, J., "Quasi-Steady Doublet-Lattice Correction for Aerodynamic Gust Response Prediction in Attached and Separated Transonic Flow," *CEAS Aeronautical Journal*, Vol. 9, No. 1, 2018, pp. 53–66. https://doi.org/10.1007/s13272-017-0273-0

[10] Watkins, C. E., Runyan, H. L., and Woolston, D. S., "On the Kernel Function of the Integral Equation Relating the Lift and Downwash Distributions of Oscillating Finite Wings in Subsonic Flow," NACA TR R-1234, 1955.

[11] Martínez, M. S.ánchez, and Dimitriadis, G., "Subsonic Source and Doublet Panel Methods," *Journal of Fluids and Structures*, Vol. 113, Aug. 2022, Paper 103624. https://doi.org/10.1016/j.jfluidstructs.2022.103624

[12] Dimitriadis, G., Panagiotou, P., Dimopoulos, T., and Yakinthos, K., "Prediction of Aerodynamic Loads and Stability Derivatives Using the Unsteady Source and Doublet Panel Method for BWB Configurations," *Proceedings of the AIAA Scitech 2024 Forum*, AIAA Paper 2024-0239, Jan. 2024. https://doi.org/10.2514/6.2024-0239

[13] Dimitriadis, G., Panagiotou, P., Dimopoulos, T., and Yakinthos, K., "Aerodynamic Stability Derivative Calculations Using the Compressible Source and Doublet Panel Method," *Journal of Aircraft*, Vol. 61, No. 4, 2024, pp. 1034–1046. https://doi.org/10.2514/1.C037747

[14] Piatak, D. J., and Cleckner, C. S., "Oscillating Turntable for the Measurement of Unsteady Aerodynamic Phenomena," *Journal of Aircraft*, Vol. 40, No. 1, 2003, pp. 181–188. https://doi.org/10.2514/2.3073

[15] Zwaan, R. J., and AGARD, Data Set 9: LANN Wing Pitching Oscillation," *Compendium of Unsteady Aerodynamic Measurements*, edited by Various, AGARD-R-702, Addendum No. 1, 1985, pp. 9-1–9-76.

[16] Economon, T. D., Palacios, F., Copeland, S. R., Lukaczyk, T. W., and Alonso, J. J., "SU2: An Open-Source Suite for Multiphysics Simulation and Design," *AIAA Journal*, Vol. 54, No. 3, 2016, pp. 828–846. https://doi.org/10.2514/1.J053813

[17] Geuzaine, C., and Remacle, J.-F., "Gmsh: A Three-Dimensional Finite Element Mesh Generator with Built-in Pre- and Post-Processing Facilities," *International Journal for Numerical Methods in Engineering*, Vol. 79, No. 11, 2009, pp. 1309–1331. https://doi.org/10.1002/nme.2579

[18] Carson Yates, E., Jr., "AGARD Standard Aeroelastic Configurations for Dynamic Response I— Wing 445.6," AGARD TR R-765, 1988.

[19] Kafkas, A., Kilimtzidis, S., Kotzakolios, A., Kostopoulos, V., and Lampeas, G., "Multi-Fidelity Optimization of a Composite Airliner Wing Subject to Structural and Aeroelastic Constraints," *Aerospace*, Vol. 8, No. 12, 2021, pp. 398. https://doi.org/10.3390/aerospace8120398

[20] Kilimtzidis, S., Kotzakolios, A., and Kostopoulos, V., "Efficient Structural Optimisation of Composite Materials Aircraft Wing," *Composite Structures*, Vol. 303, Jan. 2023, Paper 116268. https://doi.org/10.1016/j.compstruct.2022.116268

[21] Dimitriadis, G., Kilimtzidis, S., Kostopoulos, V., Laraspata, V., and Soria, L., "Flutter Calculations Using the Unsteady Source and Doublet Panel Method," *Journal of Aircraft*, 2024. https://doi.org/10.2514/1.C037891

[22] Crovato, A., Prado, A. P., Cabral, P. H., Boman, R., Terrapon, V. E., and Dimitriadis, G., "A Discrete Adjoint Full Potential Formulation for Fast Aerostructural Optimization in Preliminary Aircraft Design," *Aerospace Science and Technology*, Vol. 138, July 2023, Paper 108332. https://doi.org/10.1016/j.ast.2023.108332

[23] Stanford, B. K., and Jacobson, K. E., "Transonic Flutter Dips of the AGARD 445.6 Wing," *Journal of Aircraft*, Vol. 61, No. 2, 2024, pp. 515–522. https://doi.org/10.2514/1.C037679

[24] Hess, J. L., and Smith, A. M. O., "Calculation of Potential Flow About Arbitrary Bodies," *Progress in Aerospace Sciences*, Vol. 8, No. 1, 1967, pp. 1–138. https://doi.org/10.1016/0376-0421(67)90003-6

[25] Katz, J., and Plotkin, A., *Low Speed Aerodynamics*, Cambridge Univ. Press, Cambridge, England, U.K., 2001. https://doi.org/10.1017/CBO9780511810329

J. Vassberg
Associate Editor